université PARIS-SACLAY

Faculty of Sciences

QUARMEN ERASMUS MUNDUS JOINT MASTER

INTERNSHIP REPORT

QUANTUM HARDWARE CHARACTERISATION AND LASER SYSTEM CALIBRATION

Presented by:
David Jesús Árbol Guerrero

Academic year 2023-2024

Abstract

This report presents the work I carried out as an intern in Pasqal's System Performance team between June 3rd and July 31st, 2024, detailing the tasks and contributions made during this period. Pasqal is a quantum computing company that develops *quantum processing units* (QPUs) based on ^{87}Rb *cold neutral atoms*. The System Performance team in Pasqal plays a key role in monitoring, calibrating, and characterizing quantum hardware, ensuring its optimal operation, which is essential for the precise manipulation of cold neutral atoms.

I began by documenting the operating procedures of Pasqal's QPUs, *Fresnel 1* and *Fresnel 2*, summarising hardware components, specifications and overall functioning. I also described four procedures used to characterize the optical trap parameters. During this time, I attended the *Fresnel 1* team's weekly meetings and, in parallel, I tackled one of those discussed issues: I modelled the behaviour of an atom in an optical trap under a protocol to measure its oscillation frequency.

Next, I studied the theoretical model of the two-level system that Pasqal employs as a qubit. I reviewed an article describing a three-level system of ^{87}Rb atoms driven by two lasers, which under certain assumptions can be reduced to a two-level system. I recalculated the main results and provided a detailed derivation.

The main focus of my internship involved calibrating a new acquisition device for measuring the pulsed laser signals that excite the atoms and induce Rabi oscillations on their energy levels. These signals, square pulses, correspond to specific Rabi frequencies set by the input laser power. Pasqal uses a protocol to generate Rabi oscillations with varying frequencies (inputs), from which the pulse signal and the probability of finding the atom in the ground state are measured (outputs).

My task was to compare the measured Rabi frequencies Ω_{meas} with the input ones Ω_{input}, and to analyze the voltage signal V_{PD} aquired by the new acquisition device, V_{PD}. The goal was to establish the relations $V_{\mathrm{meas}} = f(\Omega_{\mathrm{set}})$, $\Omega_{\mathrm{real}} = g(\Omega_{\mathrm{input}})$, and $\Omega_{\mathrm{meas}} = h(V_{\mathrm{meas}})$. To do so, I designed pulse sequences on the QPU operative system and wrote Python code to characterise the signals. I successfully obtained the relation $V_{\mathrm{meas}} = f(\Omega_{\mathrm{set}})$, which followed the expected quadratic behaviour. However, due to anomalies in the square pulses and delays in QPU availability, I could not extract the remaining relations. I therefore redirected my efforts to characterizing these anomalies and identifying their possible hardware origins.

The square pulses exhibited oscillations on the plateau with a frequency that varied quadratically with the laser frequency. Additionally, the plateau power showed a similar dependence. After analyzing these effects, I identified the ALS amplifier—located between the Single-Pass (SP AOM) and Double-Pass Acousto-Optic Modulators (DP AOM)—as the source of the problem. The amplifier introduced transient oscillations before stabilizing at the target power. Furthermore, while the DP AOM causes a quadratic variation of output power with detuning, the ALS, operating in saturation mode, was expected to compensate for it but failed to do so.

In summary, this internship allowed me to engage with both theoretical and experimental aspects of quantum hardware characterization, contribute to the analysis of hardware issues, and gain hands-on experience in a cutting-edge quantum computing environment.

Contents

1   Introduction: Cold Neutral Atom QPUs

Quantum computing represents a revolutionary advancement in computational technology, leveraging the principles of quantum mechanics to process information in fundamentally new ways. At the forefront of this field, the manipulation of cold neutral atoms has emerged as a promising approach for building quantum computers. Cold neutral atoms offer long coherence times and precise control, making them ideal candidates for quantum computation.

This section presents an overview of the internal functioning of a quantum processing unit (QPU), based on the documentation work I carried out. It is divided into 4 subsections covering general knowledge about cold neutral atoms qubits, an overview of the may components of Pasqal's QPUs and their operation, support functions, and protocols to characterise the optical traps. The information in this section is based on [1] and internal summaries provided by Pasqal regarding the QPU setup.

1.1   Theoretical Background: Cold Neutral Atom Based Qubits

A qubit based on cold neutral atoms is a two-level system formed by 2 energy levels of a neutral atom that has been cooled and confined in an optical trap. Naturally, the atom has many different energy levels but it can be manipulated using precisely tuned lasers such that we perform unitary transformations involving only these two levels. Multiple atoms can be made to interact using several lasers acting on them. In the mathematical language,this corresponds to performing unitary transformations on quantum states within the tensor product of Hilbert spaces associated with single qubits. To achieve this, the atoms are set in an array—one-, two-, or three-dimensional—the *layout*, using optical traps separated by approximately micrometres to prevent unwanted interactions. Qualitatively, this is what quantum computing with cold neutral atoms means.

Some of the key properties and advantages that make this type of qubit so appealing are:

- **Identical and perfect qubits:** There is no possibility of failure when engineering the qubit as it comes from nature and all of them will have the same properties.

- **High connectivity and scalability:** To perform a quantum gate, two or more atoms must interact. This interaction can be facilitated by bringing atoms that are initially far apart closer together using optical tweezers. Moreover, scaling up the QPU simply requires increasing the number of movable tweezers and traps, while the quantum system itself remains compact, on the order of micrometres.

- **Native multiple qubit gates:** It is possible to natively implement a gate of more than 2 qubits. For example, a Toffoli gate—the 3 qubit CCNOT gate—is computed by only 7 light pulses.

- **Large lifetime and natural quantum memory:** Using appropiate atoms, the qubits have a large lifetime (on the order of seconds), which allows the execution of a large quantity of quantum gates. Furthermore, there is no need to develop separate quantum hardware for memory purposes, as atoms can be moved aside to be preserved, taking advantage of their a long lifetime.

- **Low energy consumption:** It is among the qubits that consume the least energy since only individual atoms need cooling, not a bulk of matter as in the case of superconducting qubits. This is done using an affordable and widely researched method: laser cooling.

- **Laser manipulation:** This enables simple control compared to other technologies.

- **Alkali atoms:** Alkali atoms are ideal for quantum computing. They have long-lived hyperfine levels in the internal ground state, what results in long coherence times. Many options of 2-level systems can be formed using hyperfine levels. Rydberg states—excited states with exaggerated response to electric and magnetic fields—facilitate strong atom-atom and light-atom interactions, making them perfect candidates for the $|1\rangle$ state. After computation, atoms in the excited state can be selectively removed from the trap using laser light with sufficient energy. Therefore, presence or absence of an atom corresponds to reading $|0\rangle$ or $|1\rangle$, respectively.

  What is more, the *Rydberg Blockade* effect can be exploited to implement multi-qubit quantum gates and generate entanglement. In short, two atoms in the ground state $|g\rangle$ that are close enough cannot both promote to the rydberg state $|r\rangle$ when the pair is excited with a laser pulse. Then, with a $\pi - pulse$ the pair can transition from $|gg\rangle$ to $1/\sqrt{2}(|ge\rangle + |eg\rangle)$.

On the other hand, some drawbacks are:

- **Long initial state preparation:** Filling all traps in the optical lattice is very unlikely. Hence, a larger array is initially loaded, and optical tweezers are used to rearrange atoms into a smaller, fully occupied array, which requires lengthy preparation times.

- **Long moving times and quantum gates:** While atom mobility enables long-range connectivity, it also leads to extended computation times.

There are 2 control modes for this QPU technology:

- **Analogue control:** The evolution of the atoms is given by the Hamiltonian of the atomic system. The user can then manipulate it by using different *layouts* and, therefore, the system is allowed to evolve independently. This is a resource to perform *quantum simulation*, through which the Hamiltonian is tuned to model other quantum systems whose behaviour we want to study. One of the main applications is for *drug design* and *material science*.

- **Digital control:** The evolution of the qubits are controlled by lasers that perform quantum gates. It is mainly used for *optimisation problems* or *machine learning*.

1.2   Pasqal's QPUs

In this section we present the devices that compose a QPU in Pasqal. They are divided according to their function. The main parts of the QPU are presented hereunder:

- **Register actuators:** Hardware in charge of initializing the quantum register, this is, the initial quantum state of the system (usually $|0...0\rangle$). It includes the laser cooling system, optical traps and tweezers hardware, and the electronics to monitor the process. It is reconstructed after each computation.

- **Processing actuators:** Hardware that performs quantum computation. It implies using laser pulses and electronics to control and monitor them.

- **Quantum register:** Devices that register quantum data results. They collect fluorescence light coming from the atoms that did not escape from their trap—those in the ground state. Then, a bright signal bright means $|0\rangle$, while absence of light, $|1\rangle$.

We now examine in more detail how the devices are involved in each section.

1.2.1 Register Actuators:

A thin layer of pure ^{87}Rb is heated up inside a ultra high vacuum (UHV) chamber to get a dilute atomic vapour with around 10^6 atoms in 1 mm^3. This is achieved using traps to confine the atoms and cooling lasers with the following devices:

- **Two UHV chambers connected:** The first chamber performs the first confinement of the diluted vapour. Then, it is injected into a second chamber where it is confined and the array of optical traps is built and loaded.

- **2D MOT (Magneto-Optical Trap):** Set of devices that act on the first UHV chamber to confine the atomic vapour along a single direction to enable its injection into the second chamber. It is composed by:

    - The **Rb source** and the **oven**.
    - **3 lasers** at **780 nm**, 2 for laser cooling and 1 pusher beam.
    - **Magnetic coils** to confine the atoms in the direction along which the atoms are injected.
    - **CMOS camera** (Complementary Metal-Oxide-Semiconductor) to see the shape and size of the cloud measuring the absorbed light (see Figure 1).

- **3D MOT (Magneto-Optical Trap):** Set of devices that act on the second UHV chamber to slow down and confine the atom vapor in all directions before trapping them in an optical lattice. They create a force over the atoms as $F_{3DMOT} = -\alpha v - \kappa z$, where v and z are the velocity and position of the atom; and α, κ, constants. The 3D MOT is composed by:

    - **Four lasers at 780 nm:** Two vertical counter-propagating laser beams are used, along with two horizontal beams arranged perpendicularly. These horizontal beams are reflected to form two additional counter-propagating pairs. Four-quadrant photodiodes (4QPDs) are employed to ensure precise beam alignment.

        Each laser actually consists of two superimposed beams, one slightly detuned from the other, each serving a specific purpose: *cooling* and *repumping*. The detuning arises because they address different hyperfine transitions between the $5S_{1/2}$ and $5P_{3/2}$ energy levels.

        The *cooling* mode uses *Doppler cooling* to slow the atoms down. Using a laser that is slightly detuned below an electronic transition, an atom travelling with velocity v towards a laser source is slowed down with a force $F = -\alpha v$ what gives an upper bound v in the cloud. The atom sees the laser with a higher frequency, unlike slow atoms, so it can promote and emmit a photon in a random direction, what in average slows down the ensemble.

        The *repumping* mode pumps the atom into the correct Zeeman sublevel $5S_{1/2}$ ($F = 2$, $M = 2$), the ground state we need to perform Quantum Computing.

    - **Quadrupole coils:** These confine approximately 10^6 atoms within a volume of 1 mm^3. Two pairs of anti-Helmholtz coils generate a magnetic field that varies linearly with position around the centre, inducing a Zeeman shift that also depends linearly on the atom's position. Atoms further from the centre experience smaller energy gaps between levels,
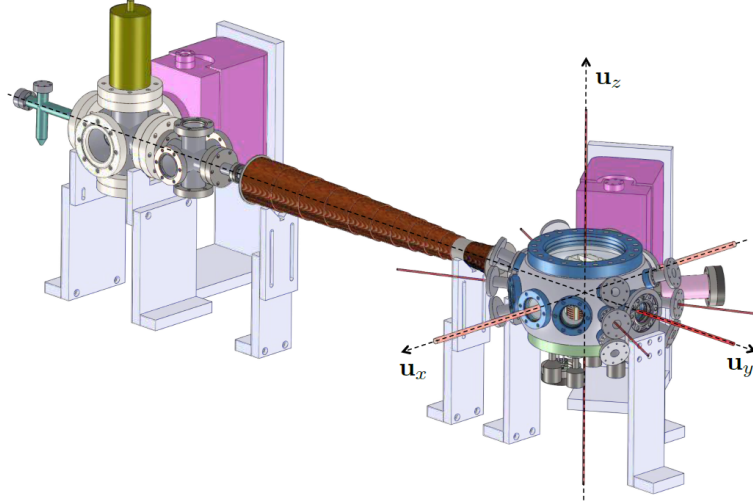
Figure 1: Scheme of the two UHV chambers and the 2D MOT and 3D MOT from [1].
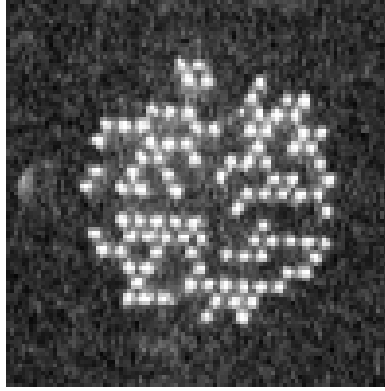

Figure 2: Atoms in the optical lattice during the loading process, before rearrangement. EMCCD camera image.

making them more susceptible to Doppler cooling transitions. As a result, these atoms are more effectively slowed down, which produces a restoring force described by $\vec{F}_{QC} = -\kappa \vec{z}$. On average, this causes the atoms to be directed towards the trap centre.

– **CMOS camera** to monitor the shape and size of the atom cloud (see Figure 1).

• **Spatial Light Modulator (SLM):** A **laser beam** at **815 nm** is sent to an **Acousto-Optic Modulator (AOM)** to control its intensity and, later, to the SLM, which uses holographic methods and diffraction techniques to create an optical trap array (layout), with a modifiable pattern. There is a 50% chance that a trap of the array is filled.

• **Two Acousto-optic laser beam deflector (AOD):** A **laser beam** at **852 nm** is sent to an AOM and, later, to the AOD. The AODs steers the moving tweezer along 2 dimensions to move an atom between two traps and generate a 2D layout with a success rate over 99%. 4Qs are used for alignment.

The signal obtained by the EMCCD camera during atom loading, prior to rearrangement, is shown in Figure 2.
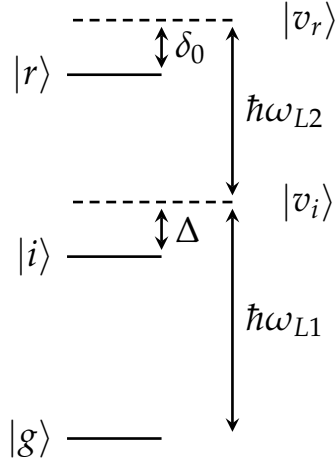
Figure 3: Level diagram of the qubits in Pasqal's QPUs. The ground state is $|g\rangle = |5S_{1/2}, F = 2, m_F = 2\rangle$, the intermediate state is $|i\rangle = |6P_{3/2}, F = 3, m_F = 3\rangle$, and the Rydberg (excited) state is $|r\rangle = |60S_{1/2}\rangle$. Two virtual states, $|v_i\rangle$ and $|v_r\rangle$, are detuned from $|i\rangle$ and $|r\rangle$, respectively. The laser frequencies ω_{L0} and ω_{L1} correspond approximately to wavelengths $\lambda_1 \approx 420\,\text{nm}$ and $\lambda_2 \approx 1013\,\text{nm}$. The first detuning frequency is $\Delta \approx 450\,\text{MHz}$, while δ_0 denotes the total detuning.

1.2.2 Processing Actuators:

To understand the devices involved in quantum computation, it is necessary to comprehend the quantum levels and the mechanisms Pasqal employs to describe and manipulate a two-level quantum system (see Figure 3). This is explained hereunder.

The magnetic field that confines the atoms induces a Zeeman effect, causing a shift in the atomic energy levels. This enables the tuning of the hyperfine structure to define an appropriate two-level system suitable for quantum computation.

In this case, Pasqal employs a three-level system that can effectively be treated as a two-level one. This approach is necessary because the ground state and the Rydberg state must serve as the logical $|0\rangle$ and $|1\rangle$, respectively, but relying on a single direct transition would require a UV laser, which is costly and challenging to detune. While detuning the laser is not strictly necessary for performing computations, it is essential for characterising certain QPU features—such as the depths of the optical traps—to ensure correct preparation of all QPU parameters.

The system consist of: the ground state $|g\rangle = |5S_{1/2}, F = 2, m_F = 2\rangle$, an intermediate state $|i\rangle = |6P_{3/2}, F = 3, m_F = 3\rangle$, and a Rydberg (excited) state $|r\rangle = |60S_{1/2}\rangle$. There are two virtual states: $|v_i\rangle$, $|v_r\rangle$, that are states detuned from $|i\rangle$ and $|r\rangle$, respectively. $\lambda_1 \approx 420$ nm and $\lambda_2 \approx 1013$ nm are the wavelengths of the lasers impinging on the atom, and Ω_1, Ω_2 their corresponding frequencies. $\Delta \approx 450$ MHz is the first detuning frequency and δ_0, the total detuning frequency (see detailed theoretical model in Section 2).

Pasqal's QPUs have two **Rydberg lasers** in charge of manipulating the quantum levels of the atoms:

- **840 nm:** Its wavelength is halved to 420 nm in a **Second-Harmonic Generation (SHG)** cavity to address the $|g\rangle \rightarrow |i\rangle$ transition. A PasqCavity feedback system adjusts the frequency precisely to the desired value; it consists of a **Fabry–Pérot cavity (F–P)** for accurate frequency measurement and a **Double-Pass AOM (DP AOM)** for frequency tuning. There is a detuning

of approximately $\Delta \approx 450$ MHz, which prevents the atom from immediately decaying to $|g\rangle$ and allows the application of the second laser to induce another transition without spontaneous emission from the intermediate state.

- **1013 nm:** It has a **PasqCavity** and a **Fabry–Pérot cavity** similar to the previous case, but without the SHG. In this stage, there is a fixed detuning δ_{fixed}, set in the same manner as before. Additionally, a more precise detuning δ_p can be introduced using a Double-Pass AOM, primarily for characterising the optical traps. Thus, the detuning of this laser is given by $\delta_{1013} = \delta_{\text{fixed}} + \delta_p$. After this stage, the beam passes through a **Double-Pass AOM**, an **ALS amplifier**, and a **Single-Pass AOM** for power modulation.

Although the total detuning is given by $\delta_0 = \Delta + \delta_{1013}$, when an atomic transition is driven by a sinusoidal electromagnetic field with detuning Δ and electric field amplitude E_0, both the ground and excited states experience an energy shift. These shifts are equal in magnitude but opposite in sign. To describe this effect, we introduce the *Rabi frequency* Ω, which depends linearly on E_0 and will be formally defined in Section 2 (see Definition 2.3). To first order in $|\Omega/\Delta|$, the energy shifts are given by:

$$\pm\frac{\Omega^2}{4\Delta}, \tag{1}$$

where the ground state is shifted downward (negative shift) and the excited state is shifted upward.

Then, assuming a level-shift (*LS*) caused only by the Rydberg lasers—since the other confining lasers are usually switched off during the computation—its theoretical value is

$$LS = \frac{\Omega_{420}^2}{4\Delta} - \alpha\frac{\Omega_{1013}^2}{4\delta_{1013}}, \tag{2}$$

where α is an empirical parameter accounting for effects related to the high density of states near the Rydberg level. This parameter can be considered constant for high detuning values used in our setuop ($\Delta, \delta_{1013} \sim 450$MHz), where the system remains well within the perturbative regime and off-resonant coupling to nearby Rydberg levels is negligible. In our case, it was measured to be $\alpha = 1.86$.

Setting $\delta_0 = 0$, which implies $\delta_{1013} = -\Delta$, the level-shift becomes

$$LS = \frac{\Omega_{420}^2 - \alpha\Omega_{1013}^2}{4\Delta}. \tag{3}$$

Assuming $\delta_p \ll \Delta$, the level-shift LS remains efectively constant, and the actual detuning is given by

$$\delta = \delta_0 + LS = \delta_0 + \frac{\Omega_{420}^2 - \alpha\Omega_{1013}^2}{4\Delta}. \tag{4}$$

Our goal is that the total detuning is controlled by δ_p.

This quantum system of a single atom can be regarded as a 2-level system (see Section 2) with a frequency transition of

$$\Omega_{\text{eff}} = \frac{\Omega_1\Omega_2}{2\Delta}. \tag{5}$$

Then the fidelity of single-qubit gates can be characterised using Rabi and Ramsey oscillations. Pasqal is currently achieving a fidelity of $\mathcal{F} > 0.995$.

1.2.3 Quantum Register:

It is composed by the devices in the section *register actuators*, which are used to "read" the quantum state of the atoms. It includes a **Electron-Multiplying Charge-Coupled Device (EMCCD) camera**, capable of detecting fluorescence photons with great efficiency. From Section 1.2.2, we know that the presence of an atom (bright signal) means reading the state $|0\rangle$ and absence (dark signal), $|1\rangle$. By using the camera along with false positive and false negative calibration functions, we can accurately determine the atomic state.

We highlight that the **FPD** (**Fast Photodiode**) and 4Qs are used to measure the power and alignment of the lasers. As with every laser, a wavemeter checks the final wavelength.

1.3 Support Functions

To achieve a good control of the quantum system we need to monitor and control well every ambient factor that might affect it:

- **Vaccum in the UHV chamber:** It must be around 10 mbar.

- **EM field controllers:** These handle the unwanted electric and magnetic fields inside the chamber that might cause energy shifts on atoms. An *electronic rack* monitors the electric field with electrodes and the magnetic field with 3 coils, 1 for each direction of space.

- **Mechanical support:** It controls vibrations and mechanical deformations of the vaccum chamber.

- **Thermal Regulation:** It monitors the temperature of the *main frame system*, *electric system*, *laser system* and the *ambient conditions*. It maintains the temperature stable using an air-water cooling with a PID (proportional integral derivative) controller. It also controls the optical core benches and the 2 Rydberg benches using a Peltier thermoelectric cooler, compensating the heat generated by the AOMs and AODs.

- **Environment:** Humidity and pressure are uncontrolled phenomena that highly affect the performance of the QPU.

- **Sequencing:** It measures the synchronisation between trapping lasers and Rydberg lasers.

- **Power supply**

- **Data management**

1.4 Optical Trap Characterization

In order to fully understand the behaviour of the atoms, it is essential to monitor and characterise the optical traps. We focus on four key features:

1.4.1 Lifetime in the Trap

The **lifetime in the trap** (τ) is the average time that the atoms remain confined in the dipole traps once the MOT lasers are switched off. Since the operation time of a computation is around 100 ms, a lifetime $\tau > 10$s is required to keep atom loss below 1%. At Pasqal, the measured lifetime is $\tau \approx 20$s, which is twice the expected according to [1] (see behaviour in Figure 4).
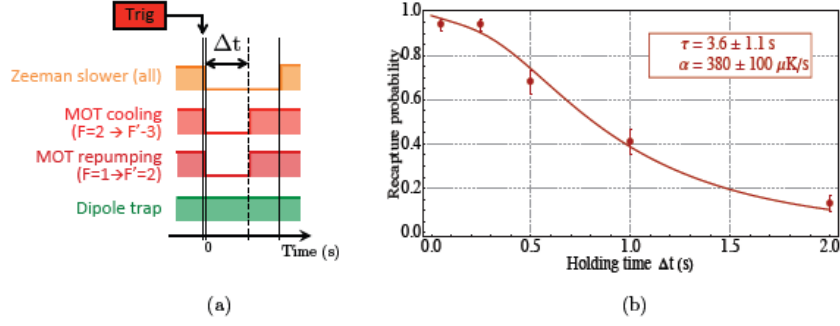
Figure 4: Lifetime trap measurements from [1].

There are two loss mechanisms:

First, losses caused by **collisions** with residual gas molecules inside the vaccum chamber, with a surviving probability of:

$$P_{coll}(t) = e^{-t/\tau}. \tag{6}$$

Second, losses due heating of the atoms, caused by the spontaneous scattering of photons impinging on the trapped atoms. According to B. Darquié [2]:

$$P_{heat}(t) = 1 - exp\left(-\frac{U_0}{k_B(T_0 + \alpha t)}\right) \cdot \left(1 + \frac{U_0}{k_B(T_0 + \alpha t)} + \frac{U_0^2}{1 k_B^2(T_0 + \alpha t)^2}\right), \tag{7}$$

where U_0 is the trap depth; and α, the heat rate, i.e., the increase in atomic temperature per second.

Then, the surviving probability is:

$$P(t) = P_{coll}(t) \cdot P_{heat}(t). \tag{8}$$

1.4.2   Single Atom Temperature

The **single atom temperature** is defined as follows. When an atom is trapped, it has a certain total energy E_i. The probability of an atom to have a particular energy is given by the thermal Boltzmann distribution, according to the experiments [3]. Thereby, the single atom temperature is defined as the temperature parameter of the distribution.

The protocol to measure the single-atom temperature is

1. Switch all the traps off except the dipole trap.

2. Switch the dipole trap off during Δt.

3. Switch the dipole trap on.

4. Switch the MOT traps on.

5. Measure the fluorescence to see the percentage of remaining atoms.

This is performed for a range of values of $\Delta t \in [0, 100]$ μs. Monte-Carlo simulations are then performed, and the simulation with the smallest mean squared error compared to the experimental data is selected (see Figure 5).
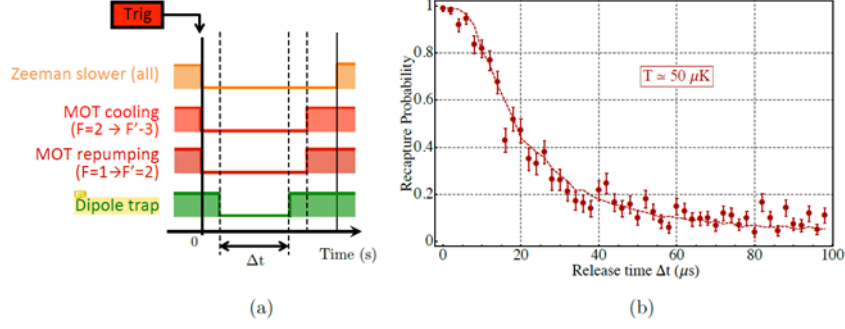
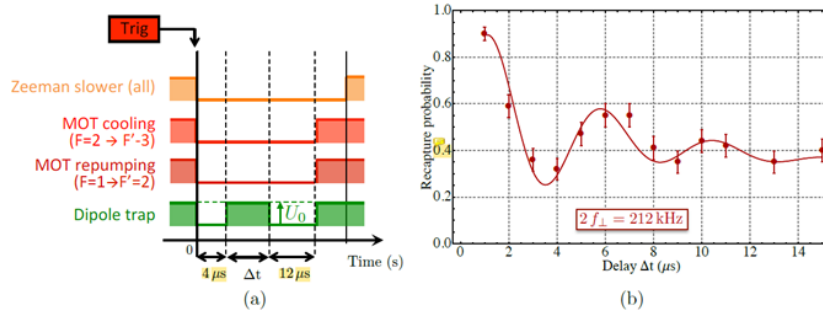Figure 5: Single atom temperature measurements from [1].

Figure 6: Atom oscillations measurements from [1].

1.4.3 Trap Oscillation Frequencies

The **trap oscillation frequencies** are the frequencies at which the atoms oscillate in the trap. To measure them:

1. Switch off all traps (both confining trap and cooling lasers) to eliminate level-shifting.

2. After a fixed time t_1 the dipole traps are switched on and off during a variable time $\Delta t = t_2 - t_1$.

3. Switch traps on again after a fixed time $t_3 - t_2$ and measure the fraction of atoms remaining in the trap (*recapture rate*).

This procedure gives a probability that oscillates with Δt, reflecting the atom oscillation frequency in the trap. This is explained in detail in Section 3. An example is shown in Figure 6.

1.4.4 Trap Depth

The **trap depth** depends on the trapping laser power. This dependence can be measured as follows. Once an atom is trapped, all the lasers are turned off except for the dipole trap and the repumping laser, which keeps the atom in the ground state $|g\rangle = |5S_{1/2}, F = 2, m_F = 2\rangle$ to prevent falling into a lower-energy state. Next, the atom is excited to the Rydberg state $|r\rangle = |60S_{1/2}\rangle$ by applying a π-pulse with a detuning δ_p using the Rydberg lasers. With a semiclassical approach and the rotating wave approximation, it can be proved that the atom population in state $|r\rangle$ as a function of δ_p has a Lorentzian profile given by

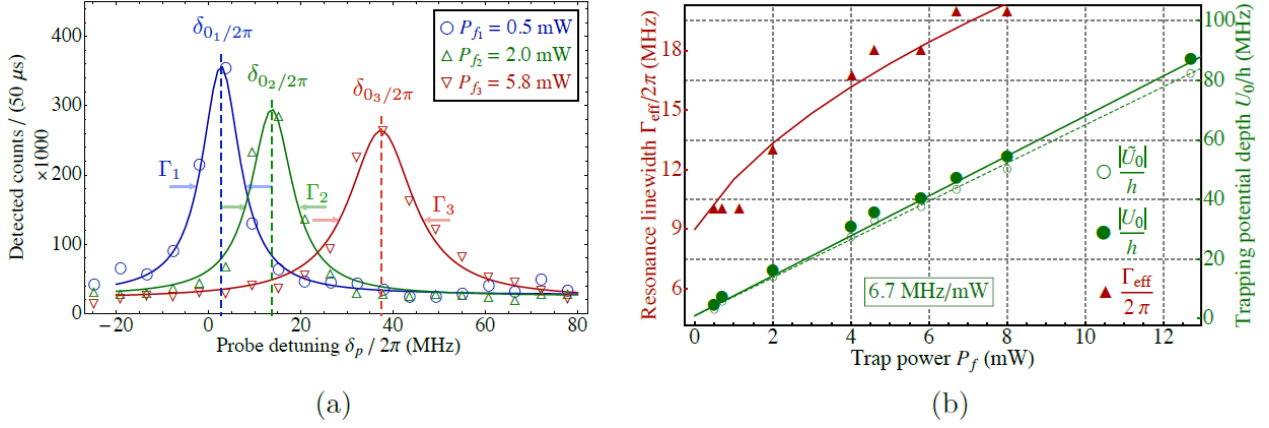$$N(t)dt = \frac{\Gamma}{2} \frac{I_p/I_{sat}}{1 + 4(\delta_p(t) - \delta_0(P_f))^2/\Gamma^2} dt, \tag{9}$$

Figure 7: Trap depth measurements from [1].

where Γ and I_{sat} parameters that depend on the atom species and transition.

The center of it (maximum at $\delta_p = \tilde{\delta}_0$) is reached when the total detuning is zero. Specifically, when $\delta_p = 0$ and there are no traps, the system is tuned such that

$$\delta = \delta_{0,Ry} + LS_{Ry} = 0, \tag{10}$$

with $\delta_{0,Ry} = \Delta + \delta_{1013} = \Delta + \delta_{fixed}$; $LS_{Ry} = 0$.

When traps and detuning are present, the total detuning becomes

$$\delta = \delta_{0,Ry} + \delta_p + LS_{Ry} + LS_{traps} = \delta_p + LS_{traps}. \tag{11}$$

By measuring the fraction of atoms in the Rydberg state as a function of δ_p, the maximum population occurs when $\delta = 0$, which implies

$$\delta_p^{max} = -LS. \tag{12}$$

This gives the energy shifting due to the optical trap potential expressed as

$$U_0/h = \delta_p^{max}/(2\pi), \tag{13}$$

where U_0 is the trap depth. See the behaviour in Figure 7.

2   Rabi Oscillations with Two-Photon Transitions: Theoretical Model

In this section, I present the theory of the Rabi oscillations using two-photon transitions in a 3-level system. It follows the article [4] and I provide detailed calculations that were omitted here.

Definition 2.1 (Two-photon transitions). *A two-photon transition is a second-order quantum mechanical process in which an atom (or another physical system) simultaneously absorbs or emits two photons, resulting in a transition between two energy states. This transition can occur via a real or virtual intermediate state, effectively constituting a two-step process. It provides a quantum model of light-matter interaction involving three energy levels.*

There are 3 types of 2-photon transitions in a 3-level system: **Λ-type**, **V-type** and **Ξ-type**, also called *cascade*-type. This depends on the shape of the transition diagram: in order, they correspond to the intermediate state being the highest, lowest, or the middle energy state, respectively. Since the treatment is the same for all of them, only the Ξ-type transition diagram is presented, as it is the one implemented in Pasqal (see Figure 8).

Definition 2.2 (State energies). *We define the ground state as the zero of energy. Accordingly, $\hbar\omega_i$ and $\hbar\omega_1$ represent the **energies of the intermediate and excited states**, respectively.*

Definition 2.3 (Rabi frequencies). *Given a 2-level system as a model of light-matter interaction with a sinusoidal coherent beam of light, it can be proved that the probability of finding the system in a state behaves as a sinusoidal function depending on the time that the laser was applied. Its frequency is the Rabi frequency (Ω):*

$$\Omega = \frac{E_0 d_{01}^{\varepsilon}}{\hbar}, \tag{14}$$

where E_0 is the electric field amplitude of the coherent laser beam; and d_{01}^{ε},

$$d_{01}^{\varepsilon} = \vec{\varepsilon}\langle 0|\vec{d}|1\rangle, \tag{15}$$

with $|0\rangle$, $|1\rangle$ the states of the system, $\vec{d} = -e\vec{r}$ the dipole operator and $\vec{\varepsilon}$ the unit vector in the direction of the electric field amplitude vector.

Definition 2.4 (Laser frequency and detuning values). *We define the following parameters:*

- *$\omega_0 = \epsilon_0/\hbar$, $\omega_i = \epsilon_i/\hbar$, and $\omega_1 = \epsilon_1/\hbar$ are the frequencies associated with the energies ϵ_0, ϵ_i, and ϵ_1 of the states $|0\rangle$, $|i\rangle$, and $|1\rangle$, respectively.*

- *ω_{L0}, ω_{L1} are the laser frequencies that drive the transitions of $|0\rangle \rightarrow |i\rangle$, and $|i\rangle \rightarrow |1\rangle$, respectively.*

- *Ω_0 and Ω_1 are the Rabi frequencies the lasers.*

- *Δ_0, Δ_1: Each transition is detuned an amount Δ_0 under and Δ_1 over the exact transition frequency but defined with the same sign.*

- *$\delta = \Delta_0 - \Delta_1$ is the total detuning.*

- *$\Delta = (\Delta_0 + \Delta_1)/2$ is the average detuning.*

Why can it be regarded as a 3-level system?
We are considering a system with $\{|0\rangle, |i\rangle, |1\rangle\}$ energy levels and transitions between them. According to the Fermi Golden Rule, $\langle j|H_I|k\rangle$ is proportional to the transition probability of $|j\rangle \leftrightarrow |k\rangle$ at first order in perturbation theory. As we can assume that every other transition is very far detuned from the laser frequency, it is very unlikely that the atom promotes to any other state.

Finally, we will consider two **assumptions** that will let us apply the adiabatic elimination method.

Definition 2.5 (Assumptions).

- *$|\Delta| \gg |\Omega_0|$, $|\Omega_1|$: This condition ensures that the intermediate state $|i\rangle$ is only weakly populated, and thus spontaneous emission from this state can be neglected. Consequently, once the atom is excited to $|i\rangle$, it is much more likely to be driven to $|1\rangle$ by the applied laser field than to decay spontaneously, since the Rabi frequencies (related to laser intensity) greatly exceed the spontaneous emission rate.*

- *$|\delta/\Delta| \ll 1$: The total detuning for the two-photon transition from $|0\rangle$ to $|1\rangle$ is small compared to the average detuning. This implies that the two-photon transition is (nearly) resonant, and the system effectively undergoes coherent oscillations between $|0\rangle$ and $|1\rangle$.*
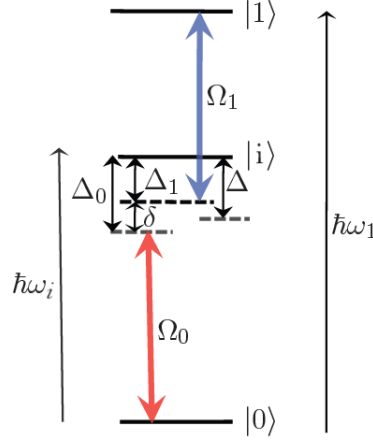
Figure 8: Ξ-type two-photon transition diagram [4]. $\hbar\omega_0$ and $\hbar\omega_1$ denote the energies of the intermediate and excited states, respectively. The Rabi frequencies Ω_0 and Ω_1, determined by the laser power, correspond to the transitions $|0\rangle \to |i\rangle$ and $|i\rangle \to |1\rangle$. The corresponding laser wavelengths are $\lambda_0 \approx 840\,\text{nm}$ and $\lambda_1 \approx 1013\,\text{nm}$, with associated laser frequencies $\omega_{L0} = c/\lambda_0$ and $\omega_{L1} = c/\lambda_0$. Each transition is detuned from resonance by Δ_0 (below) and Δ_1 (above), both defined with the same sign convention. The total two-photon detuning is given by $\delta = \Delta_0 - \Delta_1$, and the average detuning by $\Delta = (\Delta_0 + \Delta_1)/2$.

2.0.1   Definition of the Quantum System

Proposition 2.6. *We can describe the 3-level system with a Hamiltonian (H) that is sum of the atom and atom-light interaction Hamiltonians. Considering the energy reference such that $\omega_0 = 0$,*

$$H = H_{atom} + H_{AL}, \quad H_{atom} = \hbar \begin{pmatrix} 0 & 0 & 0 \\ 0 & \omega_1 & 0 \\ 0 & 0 & \omega_i \end{pmatrix}, \quad H_{AL} = \frac{\hbar}{2} \begin{pmatrix} 0 & 0 & \Omega_0 e^{i\omega_{L0}t} \\ 0 & 0 & \Omega_1 e^{i\omega_{L1}t} \\ \Omega_0^* e^{-i\omega_{L0}t} & \Omega_1^* e^{-i\omega_{L1}t} & 0 \end{pmatrix}. \quad (16)$$

Proof. From Maxwell equations, it can be proved that the Hamiltonian of a system consisting of a light beam impinging on an atom is the sum of the atom Hamiltonian plus an interaction Hamiltonian as $H = H_A + H_{AL}$ with $H_{AL} = -\hat{\vec{d}}\vec{E}$, $\hat{\vec{d}} = -e\hat{\vec{r}}$ the dipole operator and

$$\vec{E}(t) = \vec{E}_{00} \cos(\omega_{L0}t + \varphi_0) + \vec{E}_{01} \cos(\omega_{L1}t + \varphi_1), \qquad (17)$$

the electric field of the beam. The **dipole approximation** is applied here. Let us write the amplitude vector as an amplitude times a unit vector $\vec{E}_{0j} = E_{0j}\,\vec{\varepsilon}_j$. It can be proved that we reach the same result if $\varphi_i = 0$ but, to achieve this, we must define first:

Definition 2.7 $(\vec{d}_{kj}, d_{kj}^{\varepsilon})$**.**

$$\vec{d}_{kj} := \langle k|\hat{\vec{d}}_{kj}|j\rangle, \quad d_{kj}^{\varepsilon} := \langle k|\vec{\varepsilon}\,\hat{\vec{d}}_{kj}|j\rangle. \qquad (18)$$

Remark 2.8.   *i) The dipole matrix elements satisfy $d_{jk} = d_{kj}^*$. Moreover, for real dipole moments, $d_{jk} \in \mathbb{R}$.*

   ii) Since the atomic wavefunction $\psi_n(\vec{r})$ has definite parity, the probability density $|\psi_n(\vec{r})|^2$ is an even function. Given that the position operator $\hat{\vec{r}}$ is an odd function, the diagonal dipole matrix elements vanish:

$$\vec{d}_{jj} = \langle j|\hat{\vec{d}}|j\rangle = -e \int \psi_j^*(\vec{r})\,\hat{\vec{r}}\,\psi_j(\vec{r})\,d^3r = \vec{0}.$$

Now, the **rotating-wave approximation** provides a simpler Hamiltonian that approximately describes the same system.

In the interaction picture

$$H^I = e^{\frac{iH_{\text{atom}}t}{\hbar}} H \, e^{\frac{-iH_{\text{atom}}t}{\hbar}} = H^I_{\text{atom}} + H^I_{\text{AL}}. \tag{19}$$

Since H_{atom} commutes with itself, $H^I_{atom} = H_{atom}$. Moreover, using

$$e^{\frac{iH_{\text{atom}}t}{\hbar}} = \begin{pmatrix} 1 & 0 & 1 \\ 0 & e^{i\omega_1 t} & 0 \\ 0 & 0 & e^{i\omega_i t} \end{pmatrix}, \tag{20}$$

and

$$H_{\text{AL}} = -\vec{E} \sum_{j,k} \langle j|\hat{\vec{d}}|k\rangle |j\rangle\langle k| = -\vec{E} \begin{pmatrix} 0 & \vec{d}_{01} & \vec{d}_{0i} \\ \vec{d}_{10} & 0 & \vec{d}_{1i} \\ \vec{d}_{i0} & \vec{d}_{i1} & 0 \end{pmatrix}, \tag{21}$$

it is easy to obtain that

$$H^I_{\text{AL}} = -\vec{E} \begin{pmatrix} 0 & \vec{d}_{01}e^{i\omega_{01}t} & \vec{d}_{0i}e^{i\omega_{0i}t} \\ \vec{d}_{10}e^{i\omega_{10}t} & 0 & \vec{d}_{1i}e^{i\omega_{1i}t} \\ \vec{d}_{i0}e^{i\omega_{i0}t} & \vec{d}_{i1}e^{i\omega_{i1}t} & 0 \end{pmatrix}, \tag{22}$$

where $\omega_{jk} := \omega_j - \omega_k$.

Expanding $\vec{E}$, the matrix elements of H^I_{AL} can be written as

$$(H^I_{\text{AL}})_{jk} = \hbar \sum_{j,k} \left[\Omega^{j,k}_0 \cos(\omega_{L0}t) + \Omega^{j,k}_1 \cos(\omega_{L1}t) \right] e^{i\omega_{jk}t} |j\rangle\langle k|, \tag{23}$$

where $\Omega^{j,k}_\alpha$ are defined hereunder.

Definition 2.9 ($\Omega^{j,k}_\alpha$). *We define for $\alpha \in \{0,1\}$, and $j,k \in \{0,1,i\}$.*

$$\Omega^{j,k}_\alpha := \frac{E_{0\alpha}d^{\varepsilon_\alpha}_{jk}}{\hbar}, \quad \Omega_0 := \frac{E_{00}d^{\varepsilon_0}_{0i}}{\hbar}, \quad \Omega_1 := \frac{E_{01}d^{\varepsilon_1}_{i1}}{\hbar}. \tag{24}$$

Expressing the cosines as a sum of complex exponentials:

$$(H^I_{\text{AL}})_{jk} = \hbar \sum_{j,k} \left[\Omega^{j,k}_0 \frac{1}{2} \left(e^{i(\omega_{jk}-\omega_{L0})t} + e^{i(\omega_{jk}+\omega_{L0})t} \right) + \Omega^{j,k}_1 \frac{1}{2} \left(e^{i(\omega_{jk}-\omega_{L1})t} + e^{i(\omega_{jk}+\omega_{L1})t} \right) \right] |j\rangle\langle k|. \tag{25}$$

Now, we introduce the **rotating-wave approximation** in the equation (25).

Definition 2.10 (Rotating-wave approximation). *Consider the three-level system with states labeled by $\{0,1,i\}$ and transition frequencies $\omega_{jk} = \omega_j - \omega_k$, $\forall j,k \in \{0,1,i\}$. We assume that the two laser frequencies ω_{L0} and ω_{L1} are distinct and satisfy:*

- *ω_{L0} is near resonance with the transition ω_{i0},*

- *ω_{L1} is near resonance with the transition ω_{1i},*

- *both ω_{L0} and ω_{L1} are far detuned from ω_{01}.*

Formally, this means that for all $j, k \in \{0, 1, i\}$ and $\alpha \in \{0, 1\}$,

$$|\omega_{i0} - \omega_{L0}|, \quad |\omega_{1i} - \omega_{L1}| \ll |\omega_{jk} \pm \omega_{L\alpha}|, \tag{26}$$

for any other combination of indices j, k, α (ignoring sign changes).

As a consequence, the terms oscillating at frequencies $\omega_{jk} \pm \omega_{L\alpha}$ (other than the near-resonant ones) are rapidly oscillating and average to zero on any appreciable time scale. This allows us to neglect them when integrating the Schrödinger equation in the interaction picture. Hence, the interaction Hamiltonian simplifies to

$$H_{AL}^I = \frac{\hbar}{2} \begin{pmatrix} 0 & 0 & \Omega_0 e^{i(\omega_{L0} - \omega_{i0})t} \\ 0 & 0 & \Omega_1 e^{i(\omega_{L1} - \omega_{1i})t} \\ \Omega_0^* e^{-i(\omega_{L0} - \omega_{i0})t} & \Omega_1^* e^{-i(\omega_{L1} - \omega_{1i})t} & 0 \end{pmatrix}, \tag{27}$$

Finally, returning to the Schrödinger picture, we obtained the desired matrix H_{AL}.

<div align="right">□</div>

2.0.2   System in the Interaction Picture

The Hamiltonian is time-dependent in the interaction picture when it is split as $H = H_{\text{atom}} + H_{AL}$, considering H_{AL} as the interaction part. However, it is often advantageous to redefine this splitting in a different way. This alternative choice allows us to work with an interaction-picture Hamiltonian that is effectively time-independent and therefore easier to handle.

Remark 2.11. *In the interaction and Schrödinger pictures, the absolute value of the wavefunction coefficients are the same.*

Definition 2.12 (H_0, H_I). *The Hamiltonian of the three-level system composed by the atom and two lasers can be expressed as*

$$H = H_0 + H_I \tag{28}$$

$$H_0 = \hbar \begin{pmatrix} \delta/2 & 0 & 0 \\ 0 & \omega_1 - \delta/2 & 0 \\ 0 & 0 & \omega_i - \Delta \end{pmatrix} \tag{29}$$

$$H_I = \hbar \begin{pmatrix} -\delta/2 & 0 & \frac{\Omega_0}{2} e^{i\omega_{L0}t} \\ 0 & \delta/2 & \frac{\Omega_1}{2} e^{i\omega_{L1}t} \\ \frac{\Omega_0^*}{2} e^{-i\omega_{L0}t} & \frac{\Omega_1^*}{2} e^{-i\omega_{L0}t} & \Delta \end{pmatrix} \tag{30}$$

Proposition 2.13. *The Hamiltonian in the interaction picture is:*

$$H^I = e^{\frac{iH_0t}{\hbar}} H\, e^{\frac{-iH_0t}{\hbar}} = H_0^I + H_I^I, \tag{31}$$

$$H_0^I = e^{\frac{iH_0t}{\hbar}} H_0\, e^{\frac{-iH_0t}{\hbar}} = H_0, \tag{32}$$

$$H_I^I = e^{\frac{iH_0t}{\hbar}} H_I\, e^{\frac{-iH_0t}{\hbar}} = \frac{\hbar}{2} \begin{pmatrix} -\delta & 0 & \Omega_0 \\ 0 & \delta & \Omega_1 \\ \Omega_0^* & \Omega_1^* & 2\Delta \end{pmatrix}. \tag{33}$$

Proof.

- $H_0^I = H_0$ because $[H_0, H_0]$, so $[H_0, e^{\frac{iH_0t}{\hbar}}]$ and the exponential terms cancel out.

- Regarding H_I^I, we calculate $e^{\frac{iH_0t}{\hbar}}$ and apply the definition of the interaction picture. Since H_0 is a diagonal matrix

$$e^{\frac{iH_0t}{\hbar}} = \begin{pmatrix} e^{\frac{i\delta t}{2}} & 0 & 0 \\ 0 & e^{i(\omega_1 - \frac{\delta}{2})t} & 0 \\ 0 & 0 & e^{i(\omega_i - \Delta)t} \end{pmatrix}. \tag{34}$$

Multiplying the matrices, and using the Definition 2.12 of H_I, and detuning relations from Definition 2.4, we get the desired result.

$\square$

The system evolves according to the Schrödinger equation in the interaction picture as

$$i\hbar \frac{\partial}{\partial t} \psi_I(t) = H_I^I \psi_I(t). \tag{35}$$

Therefore, $\forall j \in \{0, i, 1\}$

$$|c_j^I(t)|^2 = |\langle j|\psi_I(t)\rangle| = |\langle j|e^{iH_0t}|\psi(t)\rangle| = |c_j(t)|^2, \tag{36}$$

so it suffices to obtain $c_j^I(t)$ to get $|c_j(t)|$.

2.0.3 Adiabatic Elimination Method

To facilitate the calculations, a second approximation is applied.

Definition 2.14 (Adiabatic elimination). *The adiabatic elimination is a technique to simplify the description of a system by removing or neglecting fast-evolving oscillating degrees of freedom. Since the intermediate state $|i\rangle$ is far-detuned by $\Delta \gg \Omega_j$, $j \in \{0, 1\}$, it will remain low populated if it has no initial population $c_i(0) = 0$. Therefore, the change of the population can be approximated to zero $\partial_t c_i(t) = 0$.*

Remark 2.15. *$c_i^I(t)$ is the coefficient of the intermediate state $|i\rangle$ in the interaction-picture wavefunction.*

Using adiabatic elimination 2.14, the Schrödinger equation (35), and projecting over $|i\rangle$,

$$2i \, \partial_t c_i^I(t) = \langle i|H_I^I|\psi_I\rangle = \Omega_0^* c_0(t) + \Omega_1^* c_1(t) + 2\Delta c_0(t) = 0. \tag{37}$$

Finally, we can express the intermediate state as a linear combination of the other states:

$$c_i^I(t) = -\frac{\Omega_0^* c_0(t) + \Omega_1^* c_1(t)}{2\Delta}. \tag{38}$$

Proposition 2.16. *The adiabatic elimination yields an effective 2×2 Hamiltonian for the evolution of $|0\rangle$ and $|1\rangle$ in the interaction picture as*

$$\tilde{H}_I^I = -\frac{\hbar}{2} \begin{pmatrix} \delta + \frac{|\Omega_0|^2}{2\Delta} & \frac{\Omega_0 \Omega_1^*}{2\Delta} \\ \frac{\Omega_0^* \Omega_1}{2\Delta} & -\delta + \frac{|\Omega_1|^2}{2\Delta} \end{pmatrix}. \tag{39}$$

Proof. The evolution of a system is given by the Schrödinger equation, which depends only on the interaction Hamiltonian in the interaction picture. Using the equation (38) and applying H_I^I over a generic state

$$H_I^I \psi_I = \frac{\hbar}{2} \begin{pmatrix} -\delta & 0 & \Omega_0 \\ 0 & \delta & \Omega_1 \\ \Omega_0^* & \Omega_1^* & 2\Delta \end{pmatrix} \begin{pmatrix} c_0^I \\ c_1^I \\ c_i^I \end{pmatrix} = \begin{pmatrix} -\delta c_0^I - \frac{|\Omega_0|^2 c_0^I}{2\Delta} - \frac{\Omega_0 \Omega_1^* c_1^I}{2\Delta} \\ \delta c_1^I - \frac{\Omega_0^* \Omega_1 c_0^I}{2\Delta} - \frac{|\Omega_1|^2 c_1^I}{2\Delta} \\ 0 \end{pmatrix}. \tag{40}$$

This last vector can be expressed as a multiplication of a 2×2 matrix by a 2×1 vector as $\tilde{H}_I^I \begin{pmatrix} c_0^I & c_1^I \end{pmatrix}^T$ by neglecting the $|i\rangle$ row. □

2.0.4   Evolution of the Quantum System

After these approximations, we obtain a time-independent quantum system governed by the Schrödinger equation in the interaction picture (35) with the 2×2 effective Hamiltonian $\tilde{H}_I^I$ (39). For simplicity, the detailed calculations leading to the eigenvalues and eigenvectors are omitted.

Definition 2.17 (Eigenenergies of the atom). *The system eigenenergies are:*

$$E_\pm = -\frac{\hbar}{8\Delta} \left(|\Omega_0|^2 + |\Omega_1|^2 \right) \pm \frac{\hbar}{2} \Omega_R, \tag{41}$$

with

$$\Omega_R^2 = \left(\frac{|\Omega_0|^2 + |\Omega_1|^2}{4\Delta} \right)^2 + \frac{\delta}{2\Delta} \left(|\Omega_0|^2 - |\Omega_1|^2 \right) + \delta^2. \tag{42}$$

Definition 2.18 (Eigenvectors of the atom).

$$|-\rangle = \frac{1}{\sqrt{N_-}} \left(\frac{2\Delta}{\Omega_0^* \Omega_1} \left[\delta + \frac{|\Omega_0|^2 - |\Omega_1|^2}{4\Delta} - \Omega_R \right], 1 \right), \tag{43}$$

$$|+\rangle = \frac{1}{\sqrt{N_+}} \left(\frac{2\Delta}{\Omega_0^* \Omega_1} \left[\delta + \frac{|\Omega_0|^2 - |\Omega_1|^2}{4\Delta} + \Omega_R \right], 1 \right). \tag{44}$$

where

$$N_\pm = 1 + \frac{4|\Delta|^2}{|\Omega_0|^2 |\Omega_1|^2} \left[\delta + \frac{|\Omega_0|^2 - |\Omega_1|^2}{4\Delta} \pm \Omega_R \right]^2 \tag{45}$$

is the normalisation factor.

Finally, we can solve the Schrödinger equation (35) by diagonalizing the system of two differential equations. This is done by changing the working basis to the eigenbasis.

$$i\hbar \begin{pmatrix} \dot{c}_- \\ \dot{c}_+ \end{pmatrix} = \begin{pmatrix} E_- & 0 \\ 0 & E_+ \end{pmatrix} \begin{pmatrix} c_- \\ c_+ \end{pmatrix}. \tag{46}$$

The **general solution** is

$$|\psi(t)\rangle = K_- e^{\frac{-iE_- t}{\hbar}} |-\rangle + K_+ e^{\frac{-iE_+ t}{\hbar}} |+\rangle. \tag{47}$$

Assuming the initial conditions $c_0(t = 0) = 1$ and $c_1(t = 0) = 0$, which implies $c_0^I(t = 0) = 1$ and $c_1^I(t = 0) = 0$ up to a global phase. Taking into account that $c_0^I(t) = \langle 0|\psi(t)\rangle$ and $c_1^I(t) = \langle 1|\psi(t)\rangle$,

$$c_0^I(t) = e^{i\theta t}\left\{\cos\left(\frac{\Omega_R}{2}t\right) - i\left[\frac{\delta}{\Omega_R} + \frac{|\Omega_0|^2 - |\Omega_1|^2}{4\Delta\Omega_R}\right]\sin\left(\frac{\Omega_R}{2}t\right)\right\},\tag{48}$$

$$c_1^I(t) = -e^{i\theta t}\left[\frac{|\Omega_0|^2|\Omega_1|^2}{\Omega_R\Omega_0\Omega_1^*}\frac{1}{2\Delta}\right]\sin\left(\frac{\Omega_R}{2}t\right),\tag{49}$$

where

$$\theta = \frac{|\Omega_0|^2 + |\Omega_1|^2}{8\Delta}.\tag{50}$$

Therefore,

$$|c_1(t)|^2 = \frac{|\Omega_0|^2|\Omega_1|^2}{4\Delta^2\Omega_R^2}\frac{1}{2}\left(1 - \cos(\Omega_R t)\right).\tag{51}$$

2.0.5   Achieving Rabi Oscillations of Unit Amplitude

The amplitude of the Rabi oscillations, i.e., the maximum population of the excited state, is given by the prefactor in front of the oscillatory term. In our case, the amplitude is

$$\frac{|\Omega_0|^2|\Omega_1|^2}{4\Delta^2\Omega_R^2}.\tag{52}$$

Remark 2.19. *The amplitude satisfies*

$$0 \leq \frac{|\Omega_0|^2|\Omega_1|^2}{4\Delta^2\Omega_R^2} \leq 1.\tag{53}$$

The fist inequality is obvious. The second, follows from the fact that

$$\Omega_R^2 \geq \left(\frac{|\Omega_0|^2 + |\Omega_1|^2}{4\Delta}\right)^2, \ \forall\delta \in \mathbb{R}_0^+,\tag{54}$$

which implies that

$$\frac{|\Omega_0|^2|\Omega_1|^2}{4\Delta^2\Omega_R^2} \leq \frac{4|\Omega_0|^2|\Omega_1|^2}{(|\Omega_0|^2 + |\Omega_1|^2)^2} \leq 1,\tag{55}$$

where the last inequality follows from the Cauchy–Schwarz inequality. Equality holds when $\delta = 0$ and $|\Omega_0| = |\Omega_1|$.

Remark 2.20. *The amplitude satisfies*

$$0 \leq \frac{|\Omega_0|^2|\Omega_1|^2}{4\Delta^2\Omega_R^2} \leq 1.\tag{56}$$

The first inequality is immediate. The second follows from the fact that

$$\Omega_R^2 \geq \left(\frac{|\Omega_0|^2 + |\Omega_1|^2}{4\Delta}\right)^2, \quad \forall\delta \in \mathbb{R}_0^+,\tag{57}$$

which implies that

$$\frac{|\Omega_0|^2|\Omega_1|^2}{4\Delta^2\Omega_R^2} \leq \frac{4|\Omega_0|^2|\Omega_1|^2}{(|\Omega_0|^2 + |\Omega_1|^2)^2} \leq 1,\tag{58}$$

where the last inequality follows from the arithmetic–geometric mean inequality (or equivalently, the Cauchy–Schwarz inequality). Equality holds when $\delta = 0$ and $|\Omega_0| = |\Omega_1|$.

This result is highlighted in the following proposition.

Proposition 2.21. *If $\delta = 0$,*

i) $\quad \dfrac{|\Omega_0|^2|\Omega_1|^2}{4\Delta^2\Omega_R^2} = \dfrac{4|\Omega_0|^2|\Omega_1|^2}{(|\Omega_0|^2 + |\Omega_1|^2)^2}$, $\qquad\qquad$ *ii)* $\quad \dfrac{|\Omega_0|^2|\Omega_1|^2}{4\Delta^2\Omega_R^2} = 1 \Leftrightarrow |\Omega_0| = |\Omega_1|$.

Proof.

   i) Substituting in Ω_R according to equation (42).

   ii) Using the Cauchy-Schwartz inequality.

$\hfill\square$

Proposition 2.22. *If $\delta = \frac{|\Omega_1|^2 - |\Omega_0|^2}{4\Delta}$,*

i) $\quad \dfrac{|\Omega_0|^2|\Omega_1|^2}{4\Delta\Omega_R^2} = 1$, $\qquad\qquad\qquad\qquad$ *ii)* $\quad \Omega_R = \dfrac{|\Omega_0||\Omega_1|}{2\Delta}$.

Proof. Substituting in Ω_R according to the equation (42). $\hfill\square$

Remark 2.23. *By modulating the total detuning δ so that it satisfies the condition in Proposition 2.22, it is possible to achieve Rabi oscillations with unit amplitude without requiring $\Omega_0 = \Omega_1$.*

3   Simulation of the Trap Oscillation Frequencies

3.1   Role and Objectives

During one of the weekly meetings, the team presented a series of experimental results aimed at characterising the trapping potentials. These results are discussed in [1], one of the main references guiding the team's approach to evaluating QPU performance. In particular, Section 2.3 of that article describes four fundamental parameters of the atomic traps, along with the corresponding experimental procedures for their determination. These parameters are summarised and analysed in Section 1.4 of this report.

While most of these parameters were successfully measured and interpreted, the damping behaviour associated with the atomic oscillations (as shown in Figure 6) remained partially unexplained. In response, I took the initiative to investigate this behaviour independently. The objective was to construct and simulate a theoretical model that could capture the damping features observed experimentally.

3.2   Theoretical Model and Simulation

As explained in Section 1.4.3, the oscillation frequency of an atom confined in the trap can be measured using the protocol illustrated in Figure 6.

The theoretical model used to describe this process consists of the following four stages:

1. The atom undergoes harmonic oscillation within a trapping potential at a fixed energy during the time interval $[0, t_0]$.
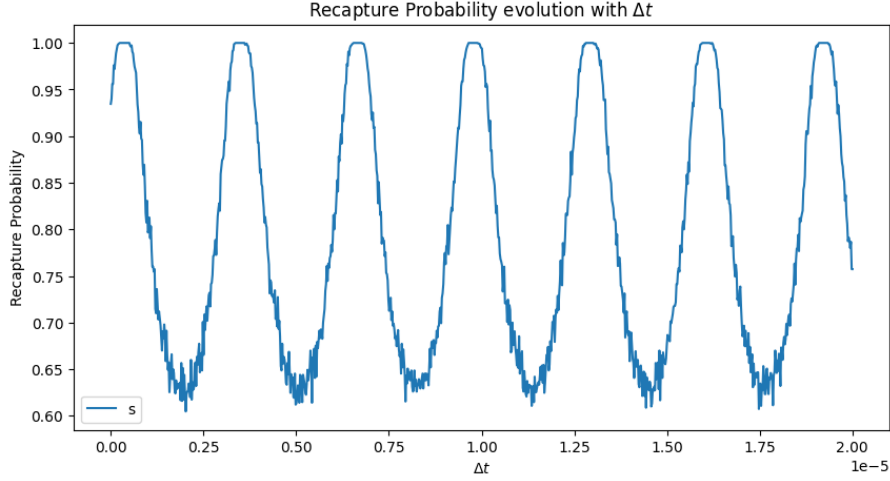
Figure 9: Monte Carlo simulation of the recapture probability used to extract the atomic oscillation frequency. A harmonic potential is applied during the intermediate step, followed by a dipole trapping potential in the final stage.

2. The trapping potential is switched off, and the atom propagates freely until time t_1.

3. A second trapping potential is activated, with possibly different characteristics, and the atom resumes oscillatory motion until time t_2.

4. Finally, the potential is turned off again, and the atom evolves freely until time t_3.

Once the dipole trap is switched off, the atom continues with constant velocity. If the duration of the free propagation phase, $t_1 - t_0$, is sufficiently long, the atom may exit the trapping region. This occurs when the kinetic energy acquired during the free evolution exceeds (in absolute value) the depth of the trapping potential. In this model, the zero of energy is defined as the energy of a free atom at rest.

Initially, I employed a harmonic oscillator potential during the intervals $t \in [0, t_0]$ and $t \in [t_1, t_2]$. However, this model did not exhibit any damping behaviour in the recapture probability (see Figure 9). This is expected, as the harmonic potential effectively corresponds to an infinite well, which does not accurately capture the finite depth of a real optical trap.

However, a dipole potential provides a more realistic description of the optical trap used in the experiment (see Figure 10):

$$U(x) = U_0\, e^{-2x^2/w^2}. \tag{59}$$

According to the article [3], the energy distribution of an atom in a trap follows the Boltzmann distribution for a given temperature. This distribution is employed to define and calculate the effective single atom temperature. Since the simulation was performed for a one-dimensional system, the energy distribution function is

$$f(E) = \frac{1}{\sqrt{2\pi E k_b T}} e^{-E/(k_b T)}. \tag{60}$$

Subsequently, a Monte Carlo simulation was conducted to determine the oscillation frequency of the atom. For a given energy, the instantaneous position and velocity of the atom at time t_0 are inherently undetermined, which make this a probabilistic problem. The initial state at t_0 is sampled
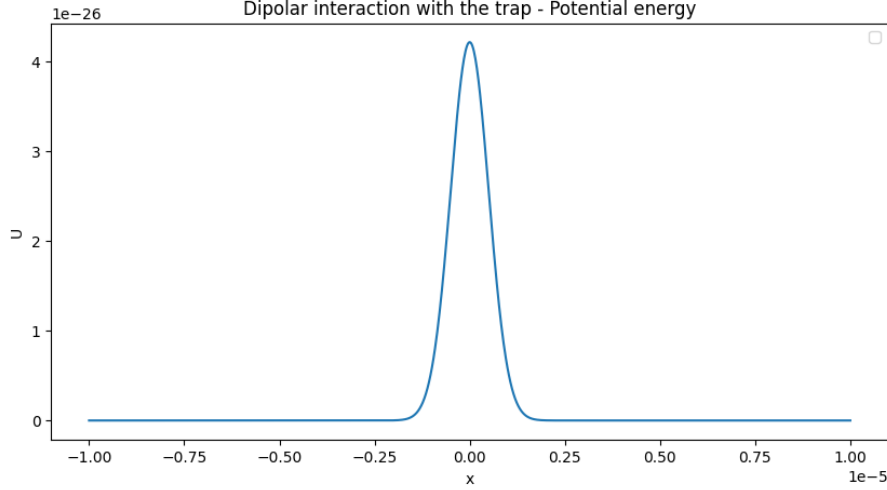
Figure 10: Dipole potential energy for $U_0 > 0$.

by placing the atom at the bottom of the potential well with a velocity corresponding to the kinetic energy $E = \frac{1}{2}mv^2$. The initial time within the oscillation period $T(E)$, which depends on the energy, is chosen uniformly at random from the interval $[0, T(E)]$.

The time evolution of each sample is then propagated up to time t_2, after which the recapture condition is evaluated. To perform the numerical integration, the Verlet algorithm was employed due to its well-known energy conservation properties and simplicity, which are essential since the escape condition depends critically on the system's energy. The simulation results are presented in Figure 11.

(a) Simulation up to time 10^{-5}s.

(b) Simulation up to time $1.4 \cdot 10^{-5}$s.
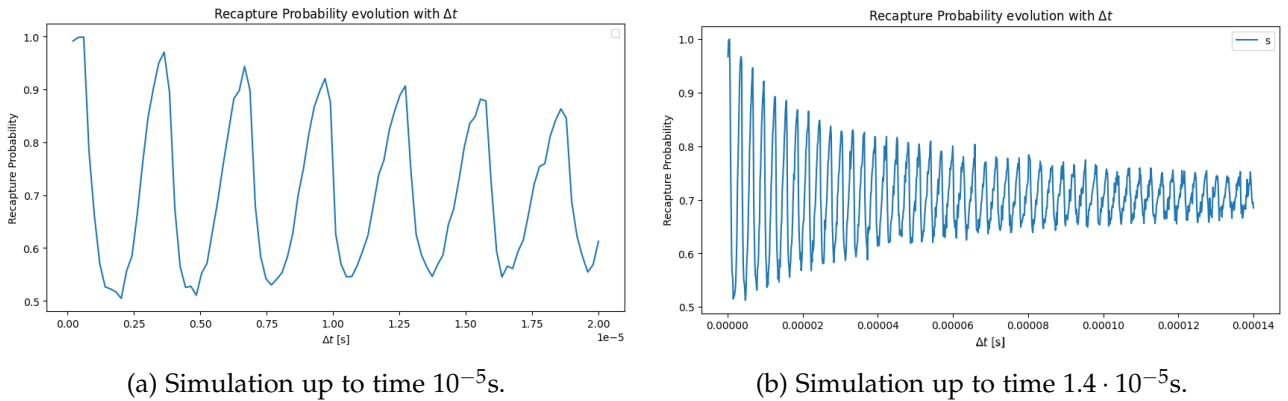
Figure 11: Monte-Carlo simulation of the recapture probability for obtaining the atom oscillation frequency using a dipole potential.

3.3   Physical Interpretation

The case in which the harmonic potential was used did not show any damping because there is no particle loss before the measurement. Consequently, tthe recapture probability remains constant with a maximum value of 1, since no atom can escape the infinite potential well (see Figure 9).

On the other hand, for the dipolar potential,two 2 main behaviours were identified.

1. **Oscillations:** First, the atoms (represented as points in phase space: position-velocity) rotatate
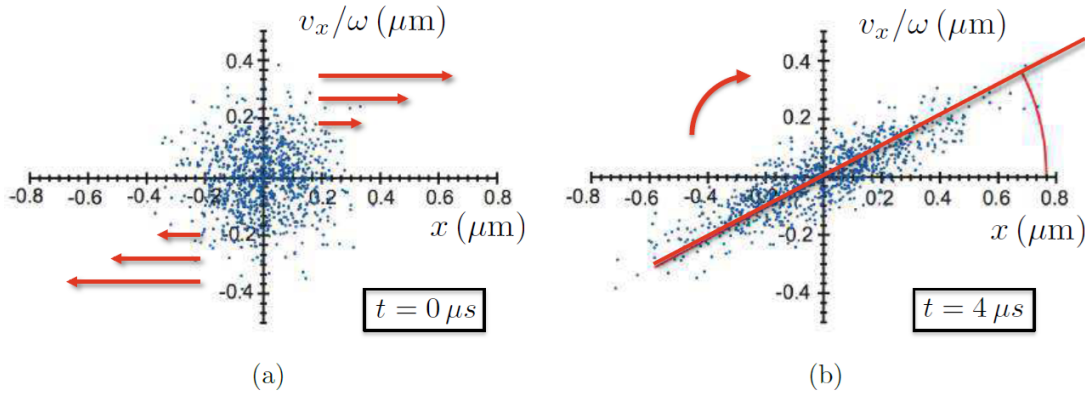
Figure 12: Phase diagram in the measurement of atom oscillation frequencies [1].

due to the confining potential. When the dipolar trap is switched off, the atoms preserve their velocity, resulting into a spread along the position axis in the phase-space diagram. This evolution describes an ellipse. When the trap is reactivated, the points resume their rotation (see Figure 12).

The recapture probability reaches a maximum when the major axis of the ellipse is aligned horizontally (indicating that atoms are close to the trap centre), and a minimum when it is vertical (indicating large spatial dispersion). These oscillations reflect the characteristic frequency of atomic motion within the trap. If the time interval $t_3 - t_2$ is sufficiently long, faster atoms will have travelled farther from the centre. Thus, at time t_3, they retain both high kinetic energy (due to conservation) and high potential energy (due to their distance from the trap centre).

Equivalent explanation: The probability of finding a particle in the dipolar trap is very high for maximum positions at any moment, because their velocities here are minimum. Then, during the off periods of the trap, these bunches of possible particle positions move slowly towards the center or out the trap (depending the direction of their velocities). When the trap is switched on, the particles start oscillating again but with more spread energies. After switching off a second time, if the time $t_2 - t_1$ is such that this bunch of atoms is at the center in t_2, they will escape from the well with high energy if $t_3 - t_2$ is long enough to let them escape. This is because in the second time we switch the trap on, the particles in the bunch will have a big kinetic energy and they will be very far from the trap center so, they will also have a big potential energy, and they escape. This minimum recapture probability is repeated over time with the atom oscillation frequency as $\Delta t = t_2 - t_1$ changes.

2. **Equivalent explanation:** The probability of finding a particle near the turning points in the dipolar trap is high, as their velocity is minimal at these positions. During the intervals when the trap is turned off, these clusters of likely atomic positions move slowly either towards the trap centre or away from it, depending on the sign of their velocity.

When the trap is switched on again, the atoms resume oscillating, but with a broader distribution of energies. After the second switching-off of the trap, if the duration $t_2 - t_1$ is such that the group of atoms reaches the centre of the trap at time t_2, and the interval $t_3 - t_2$ is sufficiently long, the atoms can escape from the trap. This occurs because, at time t_2, the atoms are at the centre with maximal velocities due to energy conservation, and after sufficient free evolution they become spatially far from the trap centre. When the trap is reactivated, they possess both large kinetic and potential energy, allowing them to overcome the trap depth
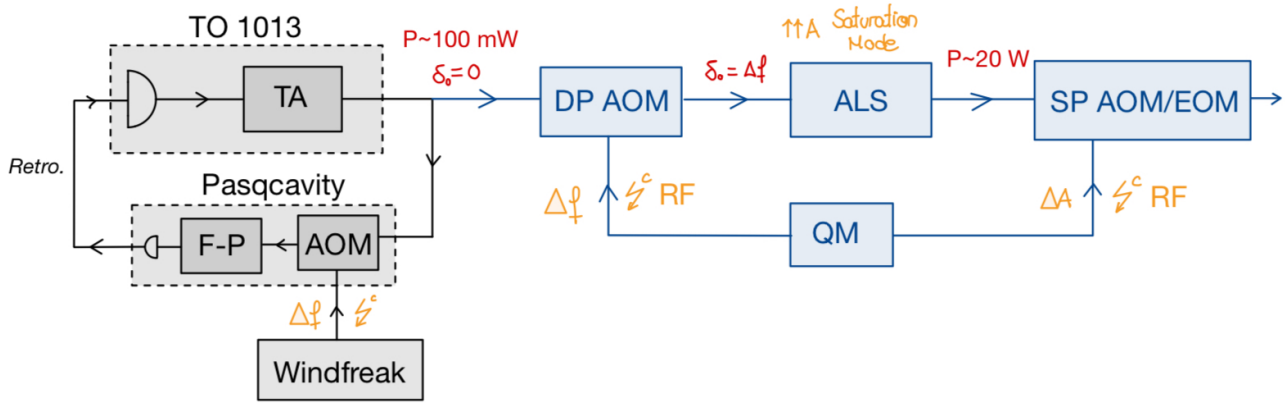
Figure 13: Laser setup scheme.

and escape. This process leads to a minimum in the recapture probability, which repeats periodically as $\Delta t = t_2 - t_1$ is varied, with a frequency corresponding to the natural oscillation frequency of the atoms in the trap.

3. **Damping:** During the off periods, the bunch of atoms located near the turning points undergoes spatial spreading. As a result, more atoms move away from the trap edges and towards the centre, where their kinetic energy is higher. Particles near the centre of the trap possess higher velocities and are thus more likely to escape if the trap remains off for a sufficiently long duration (i.e., during intervals $t_1 - t_0$ and $t_3 - t_2$).

    Consequently, a damping effect is observed in the recapture probability. Neglecting the oscillatory behaviour, the number of lost atoms depends mainly on the extent of this spatial spreading, and therefore on the durations $t_1 - t_0$ and $t_3 - t_2$. These time intervals determine the asymptotic value to which the recapture rate converges (see Figure 11).

Given the theoretical model, we can predict that the oscillation frequency observed in the recapture probability does not depend explicitly on of t_1, t_2, or t_3, but rather on the average energy of the atoms, i.e., the temperature. In contrast, the asymptotic value to which the recapture probability converges does depend on the choice of t_0, t_1, t_2, and t_3, since these parameters govern how much the atoms have spread before each recapture attempt.

We conclude that the model satisfies the experimental behaviour.

4   Acquisition Device Calibration and Anomaly Characterization

This section presents the main task I carried out during my internship at Pasqal: the characterization of the Rydberg excitation laser pulses, which are responsible for driving transitions between the quantum states of the atoms (qubits). In particular, the focus was on calibrating the acquisition system and analysing potential anomalies in the square-shaped laser pulses used to induce these transitions.

4.1   Laser System Operation

The Figure 13 shows the main components that create and manipulate the Rydberg lasers.

The **black-shaded section**, previously described in Section 1.2.2, is responsible for maintaining constant power and detuning, with target values $P \approx 100$ mW and $\delta_0 = 0$. This part of the system

is assumed to operate correctly.

The **blue section** applies a detuning to the laser using a Double-Pass AOM (DP AOM). Downstream, the ALS amplifier stabilizes the power at $P \approx 20$ W before the amplitude modulation stage. Finally, the amplitude is modulated either by a Single-Pass AOM (SP AOM) in the case of the 1013 nm beam, or by an Electro-Optic Modulator (EOM) in the case of the 420 nm beam, the latter providing shorter rise/fall times and improved resolution for short pulses.

Windfreak and *Quantum Machine* are two devices that provide a radiofrequency (RF) electric pulse to control the AOMs (detuning and amplitude modulation).

4.2 Pulse Sequence Modes

Pulse sequences can be defined on Pasqal's Operative System in two different modes: as a *one-photon transition* or a *two-photon transition*.

- **One-photon transition:** The Rydberg lasers are included independently in the sequence, and the parameters of each laser (duration, power, etc.) must be specified separately. Each laser addresses a specific transition $|0\rangle \rightarrow |i\rangle$, $|i\rangle \rightarrow |1\rangle$. In this configuration, the input power is given in units of Rabi frequency and the *Quantum Machine* hardware internally converts it to the electrical power required to drive the laser at the desired Rabi frequency.

  Instead of assuming the simplified relation of laser intensity, power, and $I = P \cdot A$, an experimentally calibrated formula is used:

  $$\Omega = \Gamma \sqrt{\frac{1}{2} \frac{I}{I_{sat}}}, \tag{61}$$

  where Γ and I_{sat} depend on the atomic species and the transition, and Ω is the power expressed as a Rabi Frequency.

- **Two-photon transition:** In this mode, both lasers are treated as if they formed a single effective laser driving the $|0\rangle \rightarrow |1\rangle$ transition directly. The pulse is defined by a global duration and a single effective Rabi frequency, which is used to calculate the combined power and detuning. The input is again expressed in units of effective Rabi frequency, as defined in Equation (5).

4.3 Measurements for Laser Characterization

To characterize the pulses, I first modified the program responsible for reading the Rydberg laser pulse data so that it could be read by the new acquisition device called *Spectrum*.

Next, I learned how to create new experimental programs in PasqOS, the operating system used to control the quantum processing unit (QPU). I designed three different square-pulse sequences to study their behavior. These programs were:

- **Red Pulse Detuning Scan:** A Double-Pass AOM (DP AOM) is used to detune the 1013 nm Rydberg laser pulse, allowing us to probe specific QPU features. This program records the laser power as a function of time for different detuning values. The measurements are taken by the *Spectrum* device, which outputs a voltage proportional to the optical power. The objective is to detect possible anomalies in the shape and stability of the square pulses under varying detunings.

- **Pulse Duration Scan:** This sequence investigates how the quality and stability of the square pulse depend on its temporal duration. The laser power is scanned for different pulse durations for both Rydberg lasers (420 nm and 1013 nm). Due to time constraints, I was unable to complete the data acquisition and thus could not carry out a detailed analysis.

- **Pulse Amplitude Scan:** This program measures the output power (in voltage units) of the laser for various input Rabi frequencies. The aim of this scan is discussed in the next section.

Theoretically, the effective Rabi frequency has a dependence given by (5) or, empirically, by (61).

However, the laser diode may emit a slightly different power from the desired one. Therefore, a calibration is required, which can be expressed as

$$(V_{meas,0}, V_{meas,1}) = f(\Omega_{input}). \tag{62}$$

The objective is to measure the experimental Rabi frequency Ω_{Rabi} by using the *Pulse Amplitude Scan* program, which allows the calibration of the effective laser power through

$$\Omega_{meas} = g(V_{meas,0}, V_{meas,1}). \tag{63}$$

By combining equations (62) and (63), we obtain the final calibration relation

$$\Omega_{meas} = h(\Omega_{input}). \tag{64}$$

Once this relation is implemented in the laser power controller, it becomes possible to apply a desired Rabi frequency without the need for direct measurement.

Note: In the end, I could not fit the function g due to time constraints and limited QPU availability, as it was being used for other tests. Consequently, the required measurements were not taken.

4.4   Data Analysis

To analyse the measured signals, I first programmed a set of Python functions to extract relevant pulse parameters: on and off times, rise and fall times, pulse duration, and the value of the constant voltage. With them, I could discern whether the noisy corresponded to valid square pulses, and conduct the previously described analyses. The parameters were defined as follows.

Definition 4.1 (On time and off time:). *These correspond to the instants at which the light signal starts and ends during a pulse sequence. Depending on the structure of the sequence, there may be multiple such events for each laser.*

Definition 4.2 (On plateau time. Off plateau time:). *The on plateau time is defined as the first instant after an on time where the signal derivative becomes zero. Analogously, the off plateau time is the last instant before an off time with zero derivative.*

Definition 4.3 (Filtered signal). *To mitigate the impact of noise, a moving average filter was applied. The filtered signal at index $i + \lfloor B/2 \rfloor$ is defined as:*

$$x^{filt}_{i+\lfloor B/2 \rfloor} = \frac{1}{B} \sum_{j=0}^{B-1} x_{i+j} \tag{65}$$

where B is the batch size, chosen to balance smoothing and signal fidelity. A signal was considered to be "on" if its voltage exceeded three times the resolution of the acquisition device (Spectrum).

Definition 4.4 (Filtered signal derivative). *The derivative of the filtered signal was estimated using finite differences:*

$$x'^{filt}_{i+\lfloor B/2 \rfloor} = \frac{1}{B}(x_{i+B} - x_i). \tag{66}$$

This derivative was considered to be zero when its absolute value was less than 10^{-4}.

4.4.1   Pulse Detuning Analysis

In Figure 14, we present three pulse measurements corresponding, respectively, to the largest negative detuning ($\delta = -62.83$ rad/μs), an approximately zero detuning ($\delta = 0.63$ rad/μs), and the largest positive detuning ($\delta = 62.83$ rad/μs).

As shown in Figure 14, a **tilting** of the plateau is observed in all pulses, despite the expected behaviour being a constant level. This tilting was identical across all measurements. Additionally, **oscillations at the plateau** were observed depending on the detuning value δ:

   i) $\delta \geq 13.32$ rad/μs: The oscillation frequency increased with δ while the amplitude remained constant.

  ii) $\delta \approx 0$ rad/μs: The plateau remains was constant.

 iii) $\delta \leq -12.06$ rad/μs: The plateau appears mostly constant, but filtered data reveals the presence of oscillations with frequencies symmetric to those observed for $\delta \geq 13.32$ rad/μs. The oscillations are around 3 times smaller.

After filtering, the oscillations can be clearly observed in Figure 15. Below, we present the data treatment applied to correct the tilting and compute the plateau mean voltage. In addition, we describe the working principle of the Double-Pass AOM to provide a possible explanation for the observed behaviour.

Tilting Analysis:
The tilting was corrected by subtracting the **linear regression** of each plateau. The slope and intercept were found to be statistically consistent across measurements, and their variations are attributed to random fluctuations within the data (standard deviation).

Plateau Mean Voltage Analysis:
From the processed data, we extracted the **mean** and **standard deviation** of the plateau voltage, as shown in Figure 16. The voltage decreases for $\delta \neq 0$ and exhibits a quadratic dependence (see Table 1). Surprisingly, the minimum is not located at $\delta = 0$ rad/μs, but around $\delta \approx -3.39$ rad/μs. This asymmetry was unexpected, as the system should behave symmetrically for positive and negative detuning values. The corresponding fitting coefficients are presented in Table 1.

Double-Pass AOM Theory:
A double-pass acousto-optic modulator (DP AOM) is used to control the frequency and intensity of a laser beam. It diffracts the beam using an acoustic wave travelling through a crystal. In the double-pass configuration, the laser passes through the AOM twice: first, it is diffracted and frequency-shifted by ΔF; then, after reflection, it passes through the AOM again, gaining a second shift of ΔF, resulting in a total shift of $2\Delta F$ [5, 6]. Oscillations could, in principle, result from interference between different diffraction modes, but this possibility is excluded in our setup due to the use of an iris that filters undesired modes.

Possible explanation for the tilting, oscillations, and voltage variations:
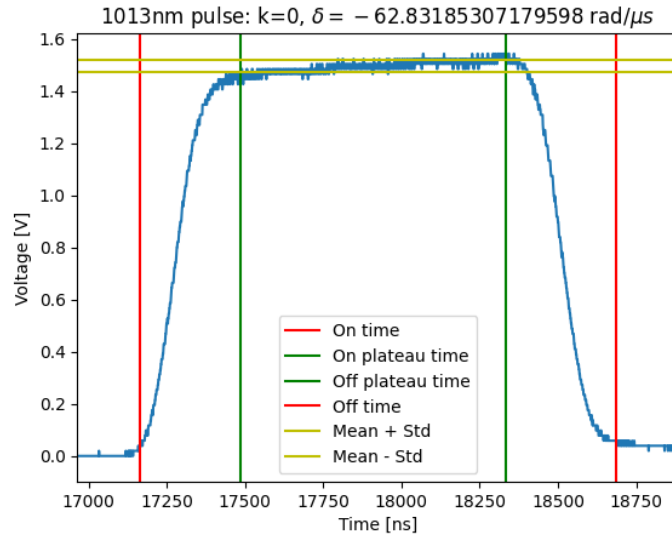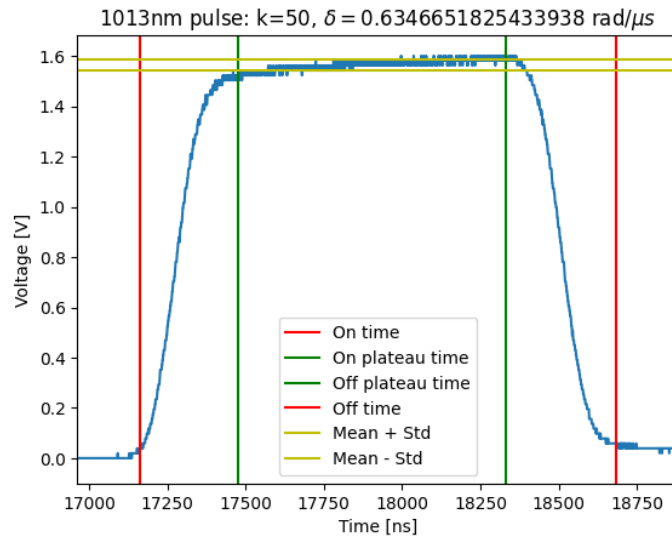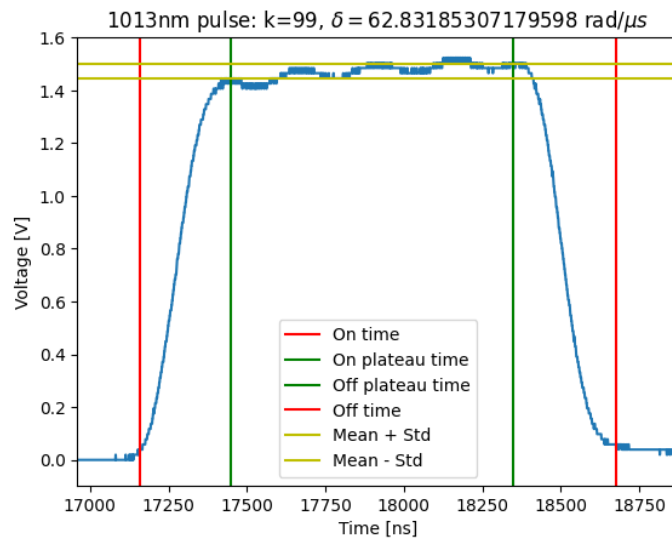The DP AOM detunes the pulse and, due to the physical mechanism, it is expected a quadratic

(a) $\delta = -62.83$ rad$/\mu s$

(b) $\delta = 0.63$ rad$/\mu s$

(c) $\delta = 62.83$ rad$/\mu s$

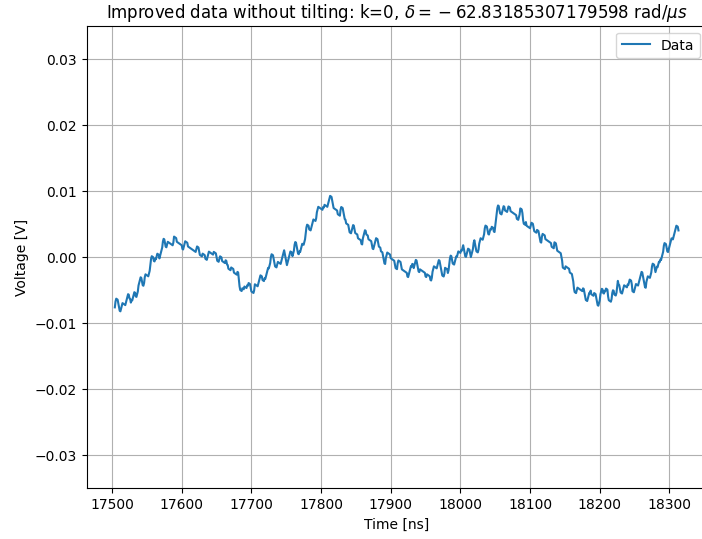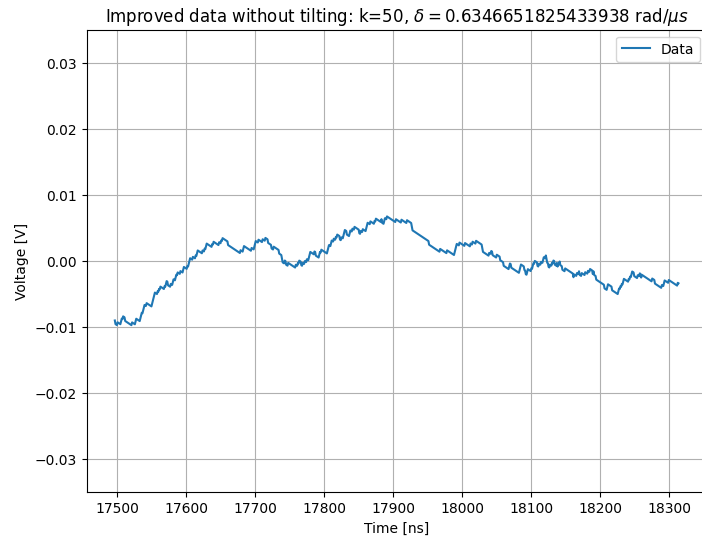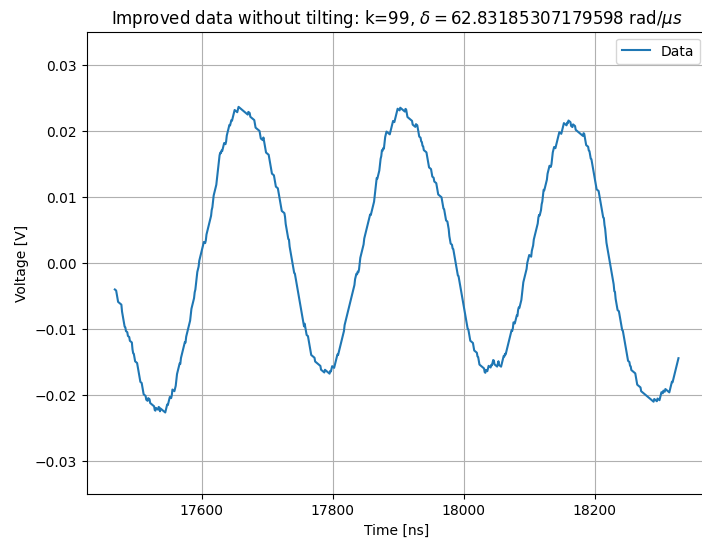Figure 14: 1013 nm: Square pulses for different input detuning values and constant amplitude.

(a) $\delta = 62.83 \text{ rad}/\mu s$

(b) $\delta = 0.63 \text{ rad}/\mu s$

(c) $\delta = 62.83 \text{ rad}/\mu s$

Figure 15: 1013 nm: Plateau oscillations for various input detuning values at constant amplitude. The data is filtered, and the tilt was removed by subtracting the linear regression from each plateau.

	1013 nm
$a_2 \; [V/(\text{rad} \,/\mu s)^2]$	$(-1.89 \pm 0.04) \cdot 10^{-5}$
$a_1 \; [V/(\text{rad} \,/\mu s)]$	$(-1.28 \pm 0.12) \cdot 10^{-4}$
$a_0 \; [V]$	$(1.5582 \pm 0.0007) \cdot 10^{-2}$

Table 1: Fitting parameters for the quadratic dependence of the voltage with the detuning for the 1013 nm laser.

and symmetric reduction of power. The ALS amplifier is responsible for keeping the light power constant by operating in saturation mode, while the SP AOM modulates the beam amplitude shape.

- Regarding the **oscillations**, it is possible that the ALS does not react fast enough to stabilise the power when the pulse is too short. In this case, the system would record the output directly from the DP and SP AOMs, without power regulation. We hypothesise that the ALS performs **damped oscillations** towards the target value, which would only be visible in longer pulses.

- Regarding the **tilting** and **voltage variations**, they might be caused by a malfunction of the ALS, since it is the only component responsible for keeping the voltage constant. The voltage reduction is likely related to the power loss introduced by the DP AOM, which remains uncorrected due to the ALS not compensating properly.

The dependence of the diffraction efficiency (I/I_0) with the radio-frequency detuning (ΔF) behaves as [6]:

$$\frac{I_1}{I_0} = \eta \; \text{sinc}^2 \left(\sqrt{\eta + \frac{\Delta\phi^2}{4}} \right), \tag{67}$$

where

$$\Delta\phi = \frac{\pi\lambda}{v} \frac{\Delta F}{2} \frac{L}{\Lambda_0}, \quad \eta = \frac{\pi^2}{2\lambda_0} M_2 \frac{L}{H} P. \tag{68}$$

The parameters are:

- I_0, I_1: Intensities of the impinging and outgoing laser sources.
- P_0, P_1: Power of the impinging and outgoing laser sources.
- H, L: Height and length of the AOM crystal.
- v, λ, λ_0: Velocity of light in the AOM crystal, wavelength inside the crystal and wavelength of the impinging laser.
- M_2: Acousto-optic figure of merit of the crystal.
- Λ_0: Wavelength of the acoustic wave in the crystal.

This is exactly the observed behaviour since $I_1/I_0 \propto P_1/P_0$. Additionally, tt can be proved that the expression (67) can be expanded around $\Delta F = 0$ as

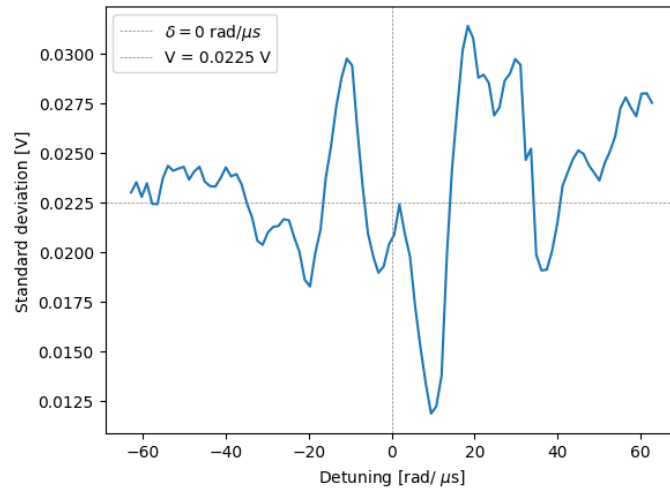$$\frac{I_1}{I_0} = a_0 + a_2 \Delta F^2 + \mathcal{O}(\Delta F^4), \tag{69}$$

which is quadratic with corrections of order $\mathcal{O}(\Delta F^4)$.
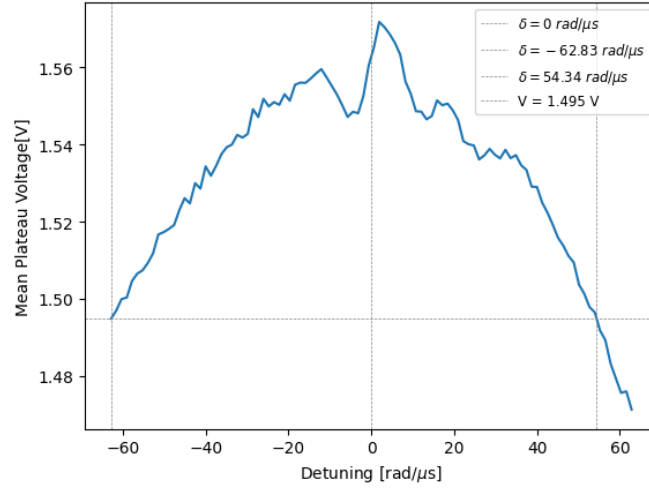
(a) Mean plateau voltage for each detuning δ.
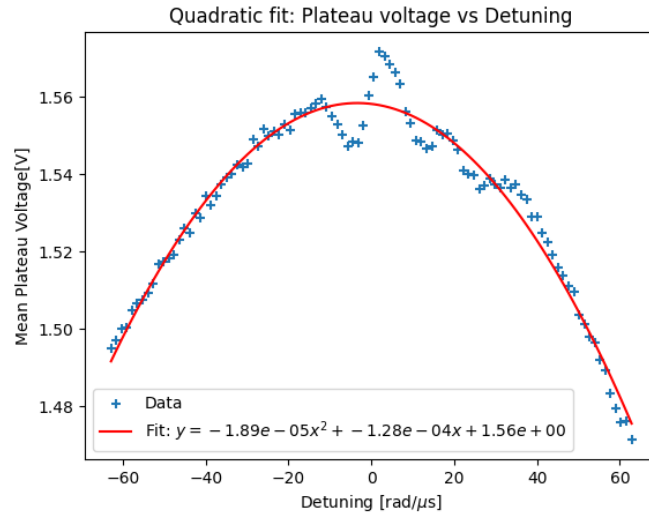
(b) Quadratic fit of mean plateau voltage values vs. detuning δ. Fitting parameters (see Eq. (71)):
$$a_2 = (1.89 \pm 0.04) \cdot 10^{-5} \text{ V}/\left(\text{rad}/\mu\text{s}\right)^2,$$
$$a_1 = (1.28 \pm 0.12) \cdot 10^{-4} \text{ V}/\left(\text{rad}/\mu\text{s}\right),$$
$$a_0 = 1.5582 \pm 0.0007 \text{ V}.$$

(c) Std. dev. of plateau voltage at each detuning δ.

Figure 16: 1013 nm: Mean and standard deviation of plateau data for each detuning value δ.

	1013 nm
a_2 [ns^{-1}/(rad /μs)^2]	$(7.71 \pm 0.12) \cdot 10^{-7}$
a_1 [ns^{-1}/(rad /μs)]	$(-4 \pm 4) \cdot 10^{-7}$
a_0 [ns^{-1}]	$(1.157 \pm 0.022) \cdot 10^{-3}$

Table 2: Fitting parameters for the quadratic dependence of the oscillations of the plateau with the detuning for the 1013 nm laser.

Dependence of Oscillation Frequencies on Detuning :

I performed a Fourier Transform (FT) over the *plateau data*. The strategy was to take the frequencies with the highest amplitudes and to plot the oscillation frequency with the detuning. However, the pulses were too small and that led to a wrong analysis.

For this reason, I performed a sinusoidal fit for all the 100 pulses as

$$f(x) = \alpha \cdot \sin(\beta x + \gamma) + b, \tag{70}$$

where b is parameter to reduce the error when obtaining the angular frequency β.

An example of a fit is shown in Figure 17a, and Figure 17b displays the oscillation frequencies as a function of detuning. The oscillation frequency exhibits a quadratic dependence and is symmetric for a detuning $\delta_c \approx 0.28$ rad/μs, which is negligible compared to the maximum detuning value $\delta = 62.83$ rad/μs (see Table 2). Moreover, the value $\delta_c = 0$ lies within the fitting error range and we can conclude that this anomaly behaves symmetrically as expected, although the origin of the quadratic dependence remains unexplained.

Explanation of Frequency Dependence on Detuning:

I suggest that the oscillation frequency is proportional to the difference of the plateau voltage with the maximum plateau voltage: $f_{osc} \propto |V - V_{max}|$. This is because the ALS performs damped oscillations of the light power until it reaches V_{max} so the oscillations have a higher amplitude and also higher oscillations if the voltage is strongly deviated from V_{max}.

4.4.2 Pulse Amplitude Analysis

In Figure 18 we show two examples of square pulses generated by the SP AOM (1013 nm) and the EOM (420 nm). It can be observed that the **EOM rise and fall times are roughly 25% to 50% of those of the SP AOM**. However, the **EOM pulse is barely constant during the plateau**. This issue must be addressed to achieve accurate quantum computing operations; meanwhile, we use these pulses only to calibrate the *Quantum Machine* as a preliminary test.

A quadratic fit was performed over the the plateau voltage versus input amplitude data. We see the fitting parameters in the Table 3 and the plot in the Figure 19, being the fitting function:
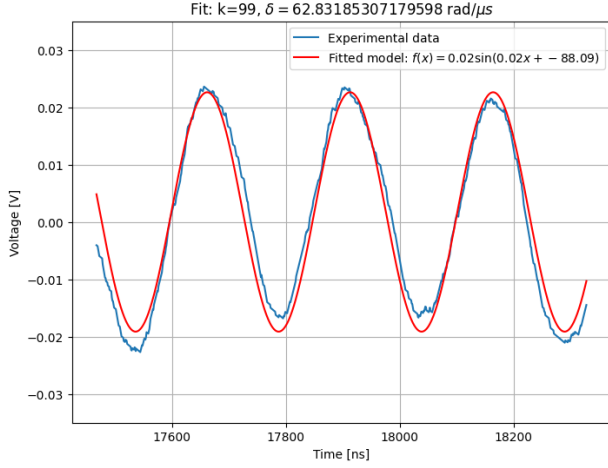
$$f(x) = a_2 x^2 + a_1 x + a_0. \tag{71}$$

The reason of this dependence is explained hereunder.

We will assume the simplistic relation:

$$P_\alpha = I_\alpha \cdot A_\alpha = \frac{c\epsilon_0 E_{0,\alpha}^2}{2} \cdot A_\alpha. \tag{72}$$

where P_α is the laser power of each beam ($\alpha \in \{0, 1\}$), $E_{0,\alpha}$ the respective electric field amplitude, I_α the intensity, and A_α the beam area.

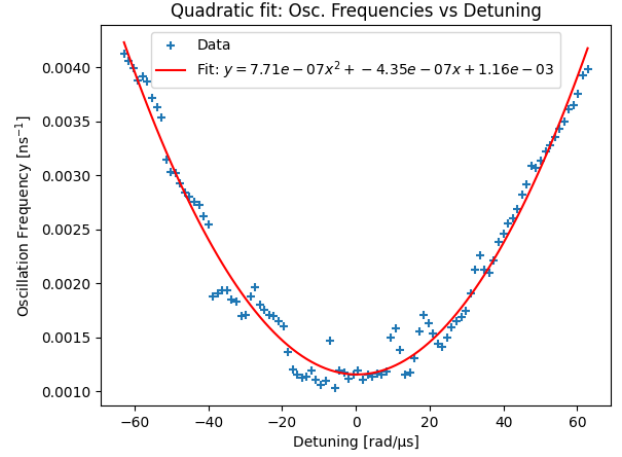(a) Sinusoidal fit for the pulse with $\delta = 62.83$ rad/μs detuning. Fitting parameters as in (70):
$\alpha = (2.087 \pm 0.014) \cdot 10^{-2}$ V,
$\beta = (2.500 \pm 0.003) \cdot 10^{-2}$ ns^{-1},
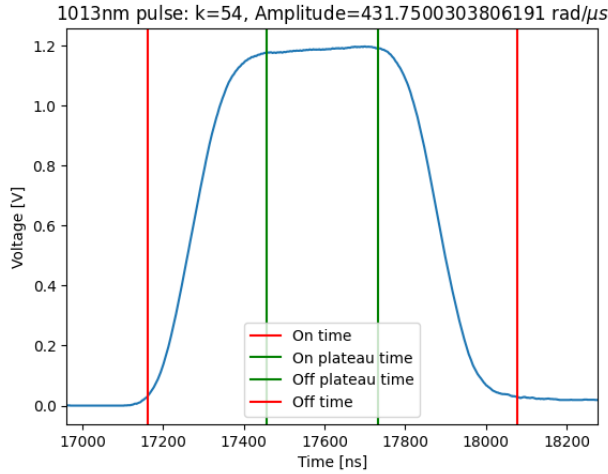$\gamma = -88.1 \pm 0.5$,
$b = (1.75 \pm 0.10) \cdot 10^{-3}$ V.

(b) Quadratic fit of the oscillation frequency with the detuning. Fitting parameters as in (71):
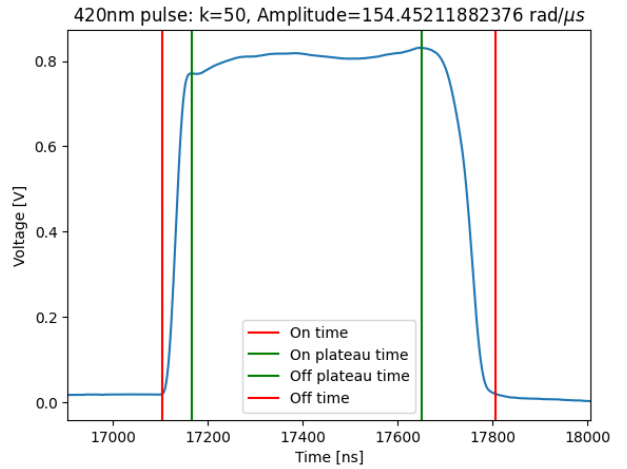$a_2 = (7.71 \pm 0.12) \cdot 10^{-7}$ ns^{-1}/ $(\text{rad}/\mu s)^2$,
$a_1 = (-4 \pm 4) \cdot 10^{-7}$ ns^{-1}/ $(\text{rad}/\mu s)$,
$a_0 = (1.157 \pm 0.022) \cdot 10^{-3}$ ns^{-1}.

Figure 17: 1013 nm: Example of a sinusoidal fit of the plateau oscillations and a fit showing the relation between the oscillation frequencies and the detuning of each pulse.

(a) Square laser pulse of 1013 nm created with the SP AOM. The optical power input is 431.75 rad/μs.

(b) Square laser pulse of 420 nm created with the EOM. The optical power input is 154.45 rad/μs.
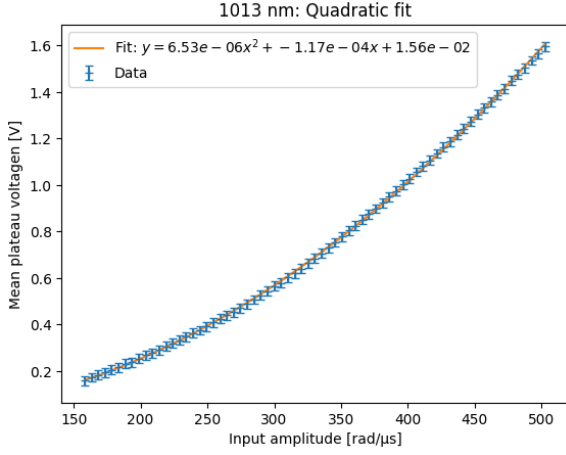
Figure 18: Square pulses with $\delta = 0$ of 1013 nm and 420 nm lasers created with a SP AOM and an EOM respectively.

From (14) and (72),

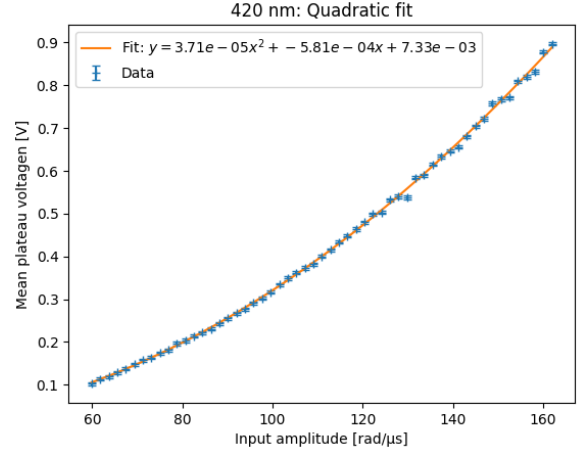$$P = \frac{1}{2} \frac{\varepsilon_0 c \hbar^2}{d_{jk}^2} A \cdot \Omega^2. \tag{73}$$

Moreover, in theory, a photodiode follows a linear relation between the impinging light power and the recorded voltage

$$P = k \cdot V, \tag{74}$$

(a) Square laser pulse of 1013 nm created with the SP AOM. The optical power input is 431.75 rad/μs.

(b) Square laser pulse of 420 nm created with the EOM. The optical power input is 154.45 rad/μs.

Figure 19: Square pulses with $\delta = 0$ of 1013 nm and 420 nm lasers created with a SP AOM and an EOM respectively.

	1013 nm	**420 nm**
$a_2 \, [V/(\text{rad}/\mu s)^2]$	$(6.53 \pm 0.07) \cdot 10^{-6}$	$(3.70 \pm 0.10) \cdot 10^{-5}$
$a_1 \, [V/(\text{rad}/\mu s)]$	$(-1.2 \pm 0.4) \cdot 10^{-4}$	$(-5.8 \pm 2.2) \cdot 10^{-4}$
$a_0 \, [V]$	$(1.6 \pm 0.7) \cdot 10^{-2}$	$(0.7 \pm 1.2) \cdot 10^{-2}$

Table 3: Fitting parameters for the quadratic dependence of the voltage with the input power.

and then,

$$I = \frac{k}{A} \cdot V = \alpha V. \tag{75}$$

Comparing these relations,

$$V = \frac{1}{2} \frac{\varepsilon_0 c \hbar^2}{d_{jk}^2} \frac{1}{\alpha} \cdot \Omega^2, \tag{76}$$

which gives the quadratic dependence. This is why the *Quantum Machine* is calibrated this way.

However, we observe that a_1 and a_0 are non-zero, which indicates a possible error in the zero-point calibration of both the voltage and the input power amplitude. Finally, if we know the required dipole operator matrix elements d_{0i} and d_{i1}, we can calibrate *Spectrum* by calculating α_{420} and α_{1013}. Even better, if the device calibration is known, we can experimentally determine the dipole operator matrix elements.

Remark 4.5 (Rabi Frequency Measurement). *It is important to highlight that the expression used to calibrate the Spectrum is different from* (14). *It is used the experimental formula* (61), *which also agrees with the quadratic behaviour observed.*

5   Conclusions

I comprehended the general map of how Pasqal's QPUs work. This gave me valuable insight into the quantum hardware used in quantum computing with cold neutral atoms and how to characterise it. In particular, I focused on the operation of the laser system and the physical mechanisms behind laser cooling, optical tweezers, and atom-light interaction.

I was able to understand the theoretical model of a 3-level system of an atom interacting with two coherent light sources. This is the model used for quantum computing in Pasqal, and I calculated the main results in detail. Starting from the dipole interaction Hamiltonian and using the rotating-wave approximation and the adiabatic elimination method, I derived the equivalent 2-level system, the probability of measuring the atom in each state, and the effective Rabi frequency.

I also worked on a theoretical model to explain the behaviour of the atom oscillations in an optical trap. A Monte Carlo simulation reproduced the same behaviour as the atom recapture rate when a laser protocol was applied to measure the oscillation frequency.

I learned to define pulse sequences with the Rydberg lasers and created new ones to characterize the square pulses. To do this, I learned new techniques to process noisy signals.

I calibrated the Spectrum device by finding a quadratic relation between the voltage of the square pulse and the input Rabi frequency received by the laser. This was as expected: the system is programmed this way since, theoretically, the Rabi frequency of an atom interacting with a laser and the light power follow this dependence.

Finally, I focused on the anomalies that the team and I found in the square pulse signals. There were oscillations at the plateau whose frequency changed quadratically with the laser detuning. The mean voltage at the plateau also changed quadratically with the detuning, although it should have remained constant. After analysing the quantum hardware that controls the lasers and gaining some insight into the behaviour of double-pass acousto-optic modulators (DP AOMs), we concluded that the issue came from a malfunction of the ALS amplifier. This amplifier is located between the Single-Pass and Double-Pass AOMs and is supposed to compensate for the quadratic variation introduced by the detuning, but it failed to do so. This explanation is consistent with our observations, although it still needs to be discussed further.

Overall, this internship helped me deepen my understanding of quantum hardware and develop both theoretical and experimental skills while contributing to a real and ongoing diagnostic task in the system.

References

[1] Lucas Beguin
Measurement of the van der Waals interaction between two Rydberg atoms.
Other [cond-mat.other]
Institut d'Optique Graduate School, 2013.
English. NNT : 2013IOTA0004.
pastel-00936072

[2] Benoît Darquié
Manipulation d'atomes dans des pièges dispolaires microscopiques et émission côntrolée de photons par un atome unique
Physique Atomique [physics.atom-ph].
Université Paris Sud - Paris XI, 2005.
Français. NNT : ff. fftel-00011604

[3] C. Tuchendler, A. M. Lance, A. Browaeys, Y. R. P. Sortais and P. Grangier
Energy distribution and cooling of a single atom in an optical tweezer
PACS numbers: 37.10.Jk, 42.50.Ct, 03.67.-a

[4] Rui HAN, Hui Khoon NG and Berthold-Georg ENGLERT;
Raman transitions without adiabatic elimination: a simple and accurate treatment
http: // dx. doi. org/ 10. 1080/ 09500340. 2013. 770573
Journal of Modern Optics, Vol. 60, No. 4, Pp. 255-265, Feb. 2013
Publisher: Informa UK Limited

[5] Kogelnik, H.;
Theory of Dielectric Waveguides
In: Tamir, T;
Theory of Integrated Optics
https: // doi. org/ 10. 1007/ 978-3-662-43208-2_ 2
Topics in Applied Physics, vol 7
Springer, Berlin, Heidelberg

[6] AA OPTO-ELECTRONIC;
Acousto-optic Theory. Application Notes.
https://pegasus-optik.de/wp-content/uploads/2019/06/AO-Theorie.pdf